UNIVERSITÁ DEGLI STUDI DI PARMA
Dottorato di Ricerca in Fisica
Ciclo XXVII

Observational Constraints on Modified Gravity Models

COORDINATORE:
Prof. CRISTIANO VIAPPIANI

TUTORS:
Prof. MASSIMO PIETRONI
Dott. LUCA GRIGUOLO

CANDIDATA:
LAURA TADDEI

Anno Accademico 2014/2015

Contents

1 Introduction **5**

2 Dark Energy **9**
2.1 Observational evidence of dark energy 9
2.2 Cosmological constant 17
2.2.1 The fine tuning problem 20
2.2.2 The coincidence problem 21
2.3 Quintessence 22
2.3.1 Further problems of minimally coupled quintessence . . 25

3 The Symmetron Model **29**
3.1 The Action 29
3.2 Screening mechanism 32
3.2.1 Static solutions 32
3.3 Constraints from tests of gravity 33

4 Non-linear evolution of cosmological perturbations **37**
4.1 Spherical collapse 37
4.1.1 Application to standard cosmologies 38
4.1.2 Application to the symmetron model 39
4.2 Halo mass function and bias 44

5 Modified gravity theories **49**
5.1 The Horndeski Lagrangian 52
5.1.1 Linear perturbation equations 53

6 Observational constraints on modified gravity **55**
6.1 A model independent approach 55
6.2 Redshift Space Distortion observations 57

6.3 Likelihood Analysis 58
6.3.1 Marginalization over σ_8 59
6.4 Current growth-rate data 61
6.4.1 Results 61
6.5 Forecast data 62
6.6 A cosmological exclusion plot 73

7 Conclusion **77**

Chapter 1

Introduction

Cosmology is a science whose goal is to study the history of the Universe through its observable properties.
From a theoretical point of view, we can think that Cosmology was born in 1917 with General Relativity (GR), a gravity theory which provides a good description of our Universe.
At that time, scientists thought that the Universe was static and finite so, in order to satisfy this assumptions, Einstein introduced a new term in his equations, the *Cosmological Constant* Λ. In fact, a static and finite Universe will collapse under the effect of gravitational interaction and the cosmological constant term can avoid this problem introducing a repulsive force that acts in opposite direction to gravity.
Today, we know that the Universe is expanding so the initial idea of a static Universe was abandoned thanks to the improvement of observational techniques that allowed to study more and more distant astrophysical sources. In fact, in 1929, the discovery of the recession motion of galaxies was a proof that the Universe was no static as they thought.
The *Standard Model of Cosmology* (ΛCDM model) is based on the assumption that the Universe is homogeneous and isotropic, at least at first approximation, on large scales (larger than O(100) Mpc), as confirmed by galaxy surveys; instead, on smaller scales, there exist large inhomogeneities, such as galaxies, clusters and superclusters.
In order to describe the evolution of the Universe, it is necessary to identify the energy components of which it is composed. With a Universe containing only non-relativistic matter and radiation and described by General Relativity, is possible to reproduce the expansion of the Universe observed by Hubble in 1929.
However, over the last decade, a wealth of evidence has been accumulated in favor of the conclusion that the expansion of our Universe has recently en-

tered in an accelerated phase that cannot be explained with ordinary matter and radiation only as components of the Universe. These evidences, which come mainly from the observation of type-Ia supernovae, from the cosmic microwave background radiation (CMB) [1] in combination with measurements of the Hubble constant and from Baryon Acoustic Oscillations (BAO), tell us that a possible explanation for the accelerated expansion is obtained by introducing a component of the cosmic fluid, the dark-energy, with an equation-of-state parameter $w < -1/3$.
For ΛCDM model, the dark energy component is described by a cosmological constant Λ which has an equation-of-state parameter $w = -1$. Nevertheless, this term is affected by serious theoretical problems connected with its interpretation that drove people to look for models alternative to the ΛCDM model.
The main reason that leads us to study alternative dark energy models or modified gravity models is that, while at the background level they behave as ΛCDM model, at linear perturbation level we can observe deviations respect to ΛCDM.
In the first part of this thesis, we will study a theory of dark energy with a screening mechanism where the dark sector is described by a scalar field with a mass of order H_0. Thanks to a discrete symmetry imposed on the scalar field, this model (which is called the *symmetron model*) is able to avoid the long-range forces of gravitational strength produced by the coupling between matter and the scalar field which are incompatible with phenomenological constraints in the laboratory or in the solar system.
Chapter 3 is focused on the Symmetron model: in particular, we review the action, the screening mechanism and the constraints from tests of gravity that we must apply in order to have a viable model.
Then, in Chapter 4, we study the gravitational clustering of spherically symmetric overdensities and the statistics of the resulting dark matter halos in the same model.
Another way to produce a late-time acceleration of our Universe is to modify General Relativity on cosmological scales: these *Modified Gravity models* need to be close to General Relativity at small scales in order to satisfy, as the Symmetron model, all the solar system tests of gravity.
In Chapter 5 we explain how it is possible to modify Einstein's equations of GR and we briefly review the most famous theories of modified gravity; finally we discuss the most general Lagrangian for the dark sector which gives only second order equations of motions. The theory described by this Lagrangian, which covers all the gravitational theories treated before, is the *Horndeski Theory*.
Finally, in Chapter 6, we focus on observational constraints that we can

obtain on modified gravity theories by using redshift space distortion observations. In addition, we want to study the cosmological constraints that we can obtain on modified gravity when the assumptions that the cosmic evolution was standard ΛCDM in the past and the present matter density and power spectrum normalization are the same as in ΛCDM model are lifted. We call this kind of approach *model-independent* approach.
At the end of Chapter 6, we produce a forecast of a cosmological exclusion plot on the Yukawa strength and range parameters, which complements similar plots on laboratory scales but explores scales and epochs reachable only with large-scale galaxy surveys.

Chapter 2

Dark Energy

2.1. Observational evidence of dark energy

Several independent observations confirm that dark energy exists.
The first signature comes from the estimation of the age t_0 of our Universe. If we take into account radiation, non-relativistic matter and dark energy and we assume that the dark energy equation of state is constant (so the dark energy density goes as $\rho_{DE} = \rho_{DE}^{(0)}(1+z)^{3(1+w_{DE})}$), we have that the expansion rate of the universe is:

$$\frac{H}{H_0} \equiv E(z) = \left[\Omega_r^{(0)}(1+z)^4 + \Omega_m^{(0)}(1+z)^3 + \Omega_{DE}^{(0)}(1+z)^{3(1+w_{DE})} + \Omega_K^{(0)}(1+z)^2\right]^{1/2} \tag{2.1}$$

The age of the Universe is given by:

$$t_0 = H_0^{-1}\int_0^\infty \frac{dz}{E(z)(1+z)} \tag{2.2}$$

For a flat universe ($\Omega_K^{(0)} = 0$) and in the case in which dark energy is described by a cosmological constant (i.e. $w_{DE} = -1$), by integrating Eq. (2.2), the age t_0 becomes:

$$t_0 = \frac{H_0^{-1}}{3\sqrt{1-\Omega_m^{(0)}}} \ln\left(\frac{1+\sqrt{1-\Omega_m^{(0)}}}{1-\sqrt{1-\Omega_m^{(0)}}}\right) \tag{2.3}$$

In the EdS universe (for which $\Omega_{DE}^{(0)} = 0$), we have that:

$$t_0 = \frac{2}{3}H_0^{-1} \approx 9.3Gyr \tag{2.4}$$

where H_0=100 h km sec^{-1} Mpc^{-1} and $h = 0.72 \pm 0.08$. So, assuming that the Universe is composed only by matter, the predicted age of the Universe is not in agreement with observational data.
We remember that an inferior limit to the age of the Universe can be placed dating the oldest known stars with low metallicity that are inside the globular clusters. So, from [2], it must be:

$$t_0 > 13.5 \pm 2Gyr$$

If we consider a Universe composed only by radiation, we obtain a lower age $t_0 = (2H_0)^{-1}$ respect to (2.4), so is not possible to take account for the observed age of the Universe with only matter and radiation.
If we assume that the Universe is composed by matter and by cosmological constant and choosing $\Omega_m^{(0)} = 0.25$, from Eq. (2.3) we obtain:

$$t_0 \approx 14.2Gyr \tag{2.5}$$

Therefore a model with matter and cosmological constant, whose energy densities are comparable, is in agreement with lower limit on the age of the Universe with globular clusters.
Another important signature of the presence of dark energy comes from Supernovae Ia.
Supernovae Ia are a type of Supernovae which do not contain a spectral line of hydrogen in their emission spectrum. They are the result of the explosion of a *white dwarf*, a star in advanced phase of life in which electrons form a degenerate gas. This kind of stars can exist only if their mass does not exceed the Chandrasekhar mass $M_C = 1.44\ M_\odot$; if the white dwarf lives in a binary system with a less evolved companion star, when the youngest star evolves into a red giant, its mass can start to flow on the white dwarf and when this reaches M_C, it explodes becoming Supernova Ia.
Most importantly, Supernovae Ia are used as *standard candles* after a proper recalibration procedure, because the absolute magnitude M is constant at the peak of brightness, so is possible to determine the luminosity distance d_L by measuring the apparent magnitude m (or luminosity) of this stars.
The luminosity distance can be obtained measuring the difference between the apparent and the absolute magnitude of a given source through the relation:

$$m - M = 5 \log_{10} d_L + 25 \tag{2.6}$$

Since for SnIa the absolute magnitude is around $M = -19$, from Eq. (2.6) is possible to relate the luminosity distance by observing the apparent magnitude m in function of the redshift z.

From a theoretical point of view, the luminosity distance is given by [3]:

$$d_L = \frac{c(1+z)}{H_0\sqrt{\Omega_K^{(0)}}} \sinh\left(\sqrt{\Omega_K^{(0)}} \int_0^z \frac{d\tilde{z}}{E(\tilde{z})}\right) \tag{2.7}$$

where $E(z)$ takes into account all the components of the Universe (see Eq. (2.1)). If we expand the function $\int_0^z d\tilde{z}/E(\tilde{z})$ around $z = 0$:

$$\int_0^z \frac{d\tilde{z}}{E(\tilde{z})} = z - \frac{E'(0)}{2} z^2 + O(z^3) \tag{2.8}$$

and we expand also the function $\sinh(x) = x + x^3/6 + O(x^5)$, we can rewrite Eq. (2.7) as follows:

$$d_L = \frac{c}{H_0}\left[z + \left(1 - \frac{E'(0)}{2}\right) z^2\right] + O(z^3) \tag{2.9}$$

When $z \ll 1$, we have $d_L \approx cz/H_0$ which is the Hubble law. From Eq. (2.9) we can also see that at high redshifts ($z \simeq O(1)$) we have deviations from Hubble law starting with terms quadratic in z.
If we define the deceleration parameter q_0 as:

$$q_0 = -\frac{1}{H_0^2}\left(\frac{\ddot{a}}{a}\right)_{t=t_0} \tag{2.10}$$

we note that we can also rewrite Eq. (2.9) in this way:

$$d_L = \frac{cz}{H_0}\left[1 + \frac{1}{2}(1 - q_0)\, z\right] + O(z^3) \tag{2.11}$$

Departures from Hubble law give a lot of information on the Universe composition since they are connected with the deceleration parameter q_0, which is, in turn, linked to cosmological parameters.
As we can even see "by eye" from Fig. (2.1), Supernovae observational data favor a Universe containing a nonvanishing dark energy component.

Another independent test for the existence of dark energy is given by the observations of the anisotropies of the temperature in the cosmic microwave background (CMB) spectrum.
The detection of the CMB radiation was the most spectacular evidence supporting the Big-Bang theory.
In 1964, an isotropic microwave radiation was discovered and through further experiments [4], it was possible to observe that this radiation has a black body spectrum (see Fig. 2.2) with a temperature of T_0=(2.725 $\pm$ 0.004) K,

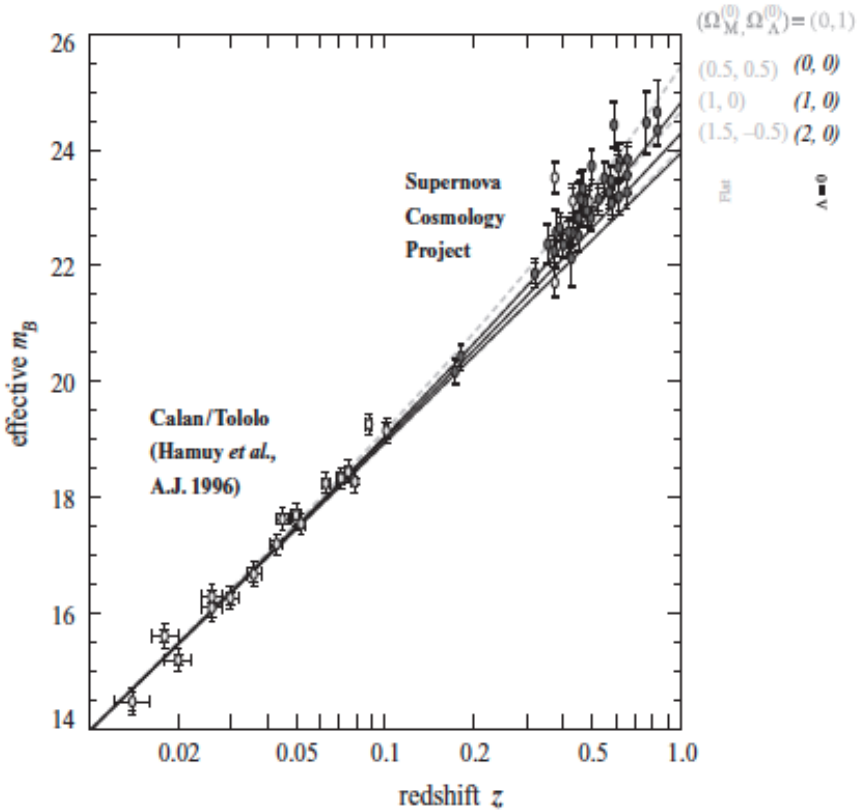

FIGURE 2.1: The solid curves show the apparent magnitude that we have from a theoretical point of view in the case in which the model is without a cosmological constant. The dashes curves correspond to the case in which the Universe is flat [3].

therefore obtaining another observational evidence of the expanding Universe model.

Indeed, after the Big Bang, the early Universe was an hot and dense medium and the photons were kept in thermal equilibrium on free electrons through processes such as the Compton scattering:

$$e^- + \gamma \longleftrightarrow e^- + \gamma \tag{2.12}$$

As the Universe expanded and cooled when the temperature became of O(eV), the electrons decoupled from the thermal bath and combined with protons to form the first hydrogen atoms:

$$e^- + p \longleftrightarrow H \tag{2.13}$$

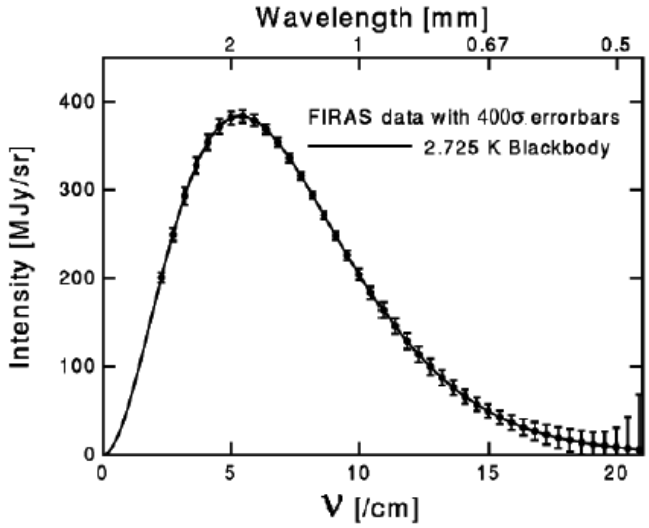

FIGURE 2.2: Black body spectrum of the CMB as detected by COBE satellite [4].

In the cosmological context this process is called *recombination*.
After recombination, the universe became transparent to photons who could then travel mostly undisturbed until today; due to the adiabatic cooling of the expansion of the Universe, the temperature of the CMB reduced by a factor $1 + z = 1100$.
The CMB radiation allows us to see back in the history of the Universe up to recombination, 380000 years after the Big-Bang. At this time, the Universe was much more homogeneous than today.
Experiments like COBE, BOOMERanG and WMAP, have measured the root mean squared temperature fluctuations around the mean value T_0 to be approximately 10^{-5}.
The measurements of temperature anisotropies opened the possibility to determine cosmological parameters with high precision. Fig. 2.3 shows the angular power spectrum of temperature anisotropies detected by WMAP.
The temperature fluctuations are connected with the presence of small density perturbations in the nearly homogeneous matter distribution of the early Universe. These matter perturbations eventually evolve during matter domination and will form the structures existing today. This is called *Sachs Wolfe effect* and it is responsible for the flat part on the left hand side in Fig. 2.3.
On scales smaller than the cosmological horizon at the time of recombination, the baryon-photon fluid (coupled together by Compton scattering) is gravitationally attracted from perturbations of dark matter and falls in its

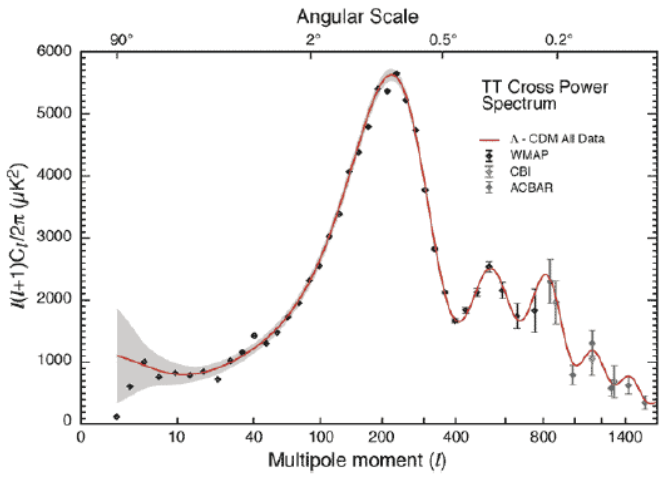

FIGURE 2.3: Angular power spectrum of temperature anisotropies detected by WMAP [5]

potential wells. When the fluid is compressed, it becomes overdense and its radiation pressure creates a force that makes it expand. Under the influence of these opposite forces (gravity and radiation pressure), the baryon-photon fluid stars making acoustic oscillations at all scales within the horizon. The acoustic oscillations are imprinted in the power spectrum as a series of peaks (see Fig 2.3) where the first one can be found at $\theta_1 \approx 1$ degrees corresponding to a multipole $l_1 \approx \pi/\theta_1 \approx 220$.
The positions of the acoustic peaks satisfy the relation

$$kr_s = n\pi \tag{2.14}$$

where n are integers and r_s is the sound horizon given by:

$$r_s(z) = \frac{c}{a_0 H_0} \int_z^\infty \frac{d\tilde{z}}{E(\tilde{z})} c_s \tag{2.15}$$

in which c_s^2 is the sound speed squared of the coupled baryon-photon plasma:

$$c_s^2 \equiv \frac{\delta P_\gamma}{\delta\rho_\gamma + \delta\rho_b} = \frac{1}{3(1+R_s)} \tag{2.16}$$

and $R_s = \frac{3}{4}\frac{\rho_b}{\rho_\gamma}$.
We define a characteristic angle θ_A connected with the position of the first peak:

$$\theta_A \equiv \frac{r_s(z_{dec})}{d_A^c(z_{dec})} \tag{2.17}$$

where d_A^c is the comoving angular distance defined as:

$$d_A^c(z) = \frac{c}{H_0\sqrt{\Omega_K^{(0)}}} \sinh\left(\sqrt{\Omega_K^{(0)}} \int_0^z \frac{d\tilde{z}}{E(\tilde{z})}\right) \tag{2.18}$$

and z_{dec} is the redshift at the decoupling era. The multipole l_A is connected with the angle θ_A by:

$$l_A = \frac{\pi}{\theta_A} = \pi \frac{d_A^c(z_{dec})}{r_s(z_{dec})} \tag{2.19}$$

We can also introduce the CMB shift parameter $\mathcal{R}$ as:

$$\mathcal{R} = \sqrt{\frac{\Omega_m^{(0)}}{\Omega_K^{(0)}}} \sinh\left(\sqrt{\Omega_K^{(0)}} \int_0^z \frac{d\tilde{z}}{E(\tilde{z})}\right) \tag{2.20}$$

and we can rewrite the multipole l_A in terms of the shift parameter:

$$l_A = \frac{\pi c}{H_0} \frac{\mathcal{R}}{\sqrt{\Omega_m^{(0)}}} \frac{1}{r_s} \tag{2.21}$$

As we can see, the position of the multipole is proportional to $\mathcal{R}$, which depends on the expansion of the Universe from the decoupling time until today. It means that the presence of a dark energy component in Eq. (2.20) leads to a shift in the position of l_A respect to the CDM model.
In a flat Universe, the shift parameter becomes:

$$\mathcal{R} = \sqrt{\Omega_m^{(0)}} \int_0^{z_{dec}} \frac{d\tilde{z}}{E(\tilde{z})} \tag{2.22}$$

where $E(z)$ is given by Eq. (2.1) with $\Omega_K^{(0)} = 0$.

Fig. 2.4 shows the shift parameter (Eq. (2.22)) for a flat universe in function of $\Omega_{DE}^{(0)}$ for two values of dark energy equation of state ($w_{DE} = -1$ and $w_{DE} = -0.5$) and by fixing $\Omega_m^{(0)} \simeq 0.3$ and $\Omega_r^{(0)} \simeq \mathrm{O}(10^{-5})$. The gray line shows the bound on $\mathcal{R}$ coming from WMAP data:

$$\mathcal{R} = 1.710 \pm 0.019 \tag{2.23}$$

For ΛCDM model ($w_{DE} = -1$), we have that $0.72 < \Omega_{DE}^{(0)} < 0.77$ for the bound given by (2.23) [3].
Finally, the detection of the baryon acoustic oscillations gives us another independent evidence of the presence of dark energy. As we said before, the

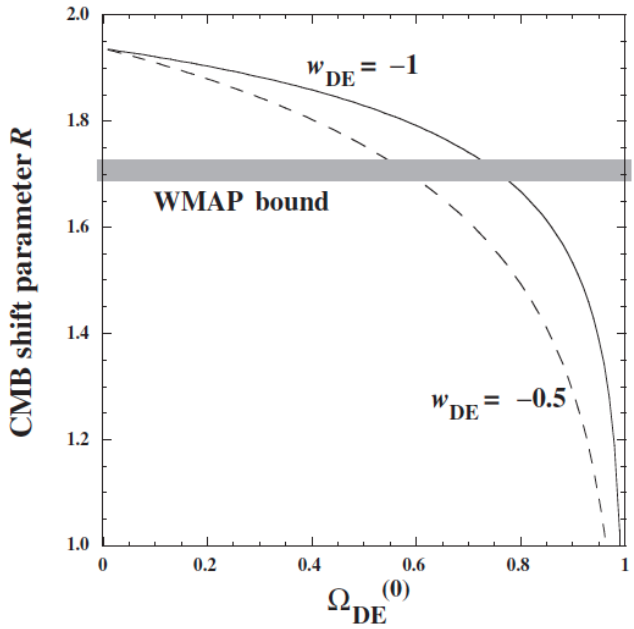

FIGURE 2.4: The CMB shift parameter in function of $\Omega_{DE}^{(0)}$ for two values of w_{DE} with the bound coming from WMAP (thick gray line) [3].

photo-baryonic fluid oscillates in the primordial plasma thanks to two opposite forces, the gravitational attraction caused by dark matter perturbations and the radiation pressure. These oscillations are frozen when photons decouple from baryons, thus at the Last Scattering Surface. This brings to the fact that a peculiar angular scale is imprinted in the temperature anisotropy of the CMB, corresponding to the sound horizon at recombination (Eq. (2.15)). When gravitational instability on baryons starts to dominate with respect to photon's pressure (which is called the *drag epoch*), it is possible to detect a preferred scale which corresponds to the sound horizon r_s at the drag epoch ($z = z_{drag}$). This effect can be observed as a bump in the two point galaxy correlation function $\xi(r)$ (which gives the excess of galaxies at a given scale with respect to a random distribution), and as oscillations (BAO) in the matter power spectrum $P(k)$:

$$P(k) = \int_{-\infty}^{+\infty} \xi(r) e^{-ikr} r^2 dr \tag{2.24}$$

Measuring these features in the directions parallel and perpendicular to the line of sight, one can determine the two quantities:

$$\delta z_s = \frac{r_s(z_{drag})H(z)}{c} \tag{2.25}$$

$$\theta_s(z) = \frac{r_s(z_{drag})}{(1+z)D_A(z)} \tag{2.26}$$

respectively.
However, current BAO data are not sensitive enough to allow a distinct measurement of these two quantities, but is possible to measure a combination of the two:

$$\left[\theta_s(z)^2 \delta z_s\right]^{1/3} \equiv \frac{r_s(z_{drag})}{\left[(1+z)^2 d_A^2(z) c/H(z)\right]^{1/3}} \tag{2.27}$$

We can also define an effective distance D_V:

$$D_V(z) \equiv \left[(1+z)^2 d_A^2(z) \frac{cz}{H(z)}\right]^{1/3} \tag{2.28}$$

Usually BAO are given in terms of the relative distance:

$$r_{BAO} \equiv \frac{r_s(z_{drag})}{D_V(z)} \tag{2.29}$$

Currently different measures of r_{BAO} are available, from the Sloan Digital Sky survey [6], the 2-Degree Field (2dF) Galaxy Redshift Survey and from WiggleZ [7]. Fig. 2.5 shows the ratio $D_V(z)/r_s(z_{drag})$ measured by Galaxy Surveys, divided by the best-fit flat ΛCDM prediction from the Planck data in function of z for ΛCDM model (black line), for a flat Universe with $w = -0.7$ (red line) and for a closed Universe with $\Omega_K^{(0)} = -0.01$ and a cosmological constant (blue line); as we can see, the observational data support the ΛCDM model.

In Fig. 2.6, we can see constraints on Ω_m and Ω_Λ from Supernovae compilation (*Union2*) ; if other probes are considered, as both CMB data (from Planck+WP) and Baryon Acoustic Oscillations (from SDSS-II, BOSS and 6dFGS), the constraints on Ω_Λ become tighter.

2.2. Cosmological constant

The simplest candidate for dark energy is the cosmological constant Λ, which is so called because its energy density is constant in time and space.

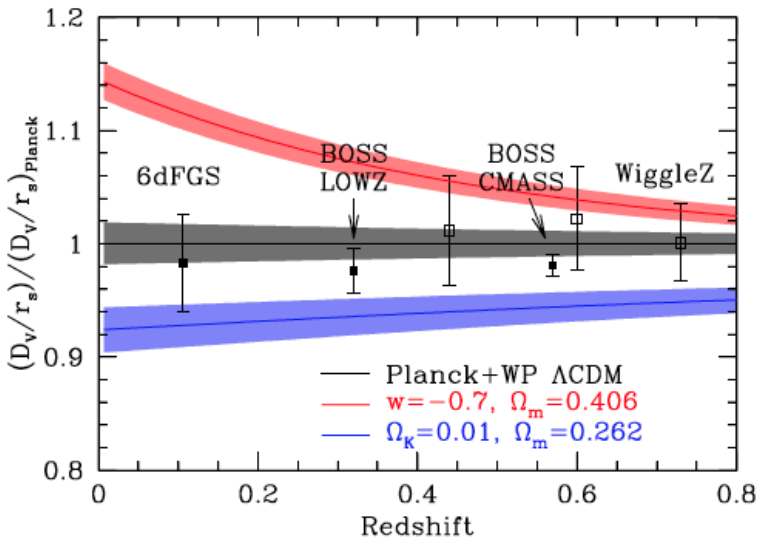

FIGURE 2.5: $D_V(z)/r_s(z_{drag})$ measured by Galaxy Surveys, divided by the best-fit flat ΛCDM prediction from the Planck data in function of z [7].

From the Einstein equations:

$$R_{\mu\nu} - \frac{1}{2}g_{\mu\nu}R = 8\pi G T_{\mu\nu} \tag{2.30}$$

the Einstein tensor $G_{\mu\nu} = R_{\mu\nu} - \frac{1}{2}g_{\mu\nu}R$ satisfies the Bianchi identities $G_{\mu\nu}{}^{;\nu} = 0$ and the energy-momentum tensor $T_{\mu\nu}$ satisfies the energy conservation law $T_{\mu\nu}{}^{;\nu} = 0$. Since the metric $g_{\mu\nu}$ is constant with respect to covariant derivatives $g_{\mu\nu}{}^{;\nu} = 0$, there is a freedom to add the term $\Lambda g_{\mu\nu}$ in the Einstein equations (2.30). Then the modified Einstein equations are given by

$$R_{\mu\nu} - \frac{1}{2}g_{\mu\nu}R + \Lambda g_{\mu\nu} = 8\pi G T_{\mu\nu} \tag{2.31}$$

By taking the trace of this equation, we find that $-R + 4\Lambda = 8\pi G T$. Combining this relation with Eq. (2.31), we obtain

$$R_{\mu\nu} - \Lambda g_{\mu\nu} = 8\pi G \left(T_{\mu\nu} - \frac{1}{2}T g_{\mu\nu} \right) \tag{2.32}$$

The modified Einstein equations (2.31) is also obtained by the action principle. We start by this action

$$S = \frac{1}{16\pi G}\int d^4x\sqrt{-g}(R - 2\Lambda) + S_m \tag{2.33}$$

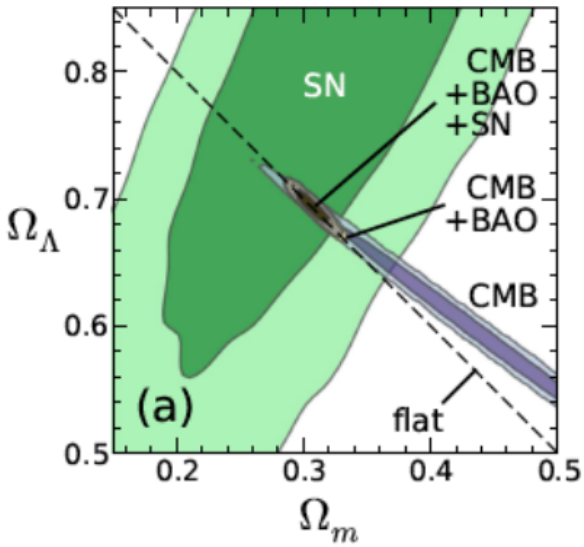

FIGURE 2.6: Observational constraints on Ω_m and Ω_Λ [8].

where $R = g^{\mu\nu} R_{\mu\nu}$ is the Ricci scalar and S_m is the matter action. If we take the variation of the action (2.33) with respect to $g^{\mu\nu}$, we obtain the Einstein equations (2.31).
In the Friedmann-Lemaitre-Robertson-Walker (FLRW) metric, given by

$$ds^2 = -dt^2 + a^2(t)\left(\frac{dr^2}{1-Kr^2} + r^2 d\theta^2 + r^2 \sin^2\theta d\phi^2\right) \tag{2.34}$$

the modified Einstein equations (2.31) give

$$H^2 = \frac{8\pi G}{3}\rho - \frac{K}{a^2} + \frac{\Lambda}{3} \tag{2.35}$$

$$\left(\frac{\ddot{a}}{a}\right) = -\frac{4\pi G}{3}(\rho + 3p) + \frac{\Lambda}{3} \tag{2.36}$$

where $a = a(t)$ is the scale factor and K is a constant curvature.
Eq. (2.36) shows that the cosmological constant contributes negatively to the pressure term and hence exhibits a repulsive effect.
Let us consider a static Universe (a = const) in the absence of Λ. Setting $H = 0$ and $\ddot{a}/a = 0$ in Eqs. (2.35) and (2.36), we find

$$\rho = -3p = \frac{3K}{8\pi G a^2} \tag{2.37}$$

Equation (2.37) shows that either ρ or p needs to be negative. When Einstein first tried to construct a static Universe, he considered that the above solution

is not physical and so added the cosmological constant to the original Einstein field equations.
Using the modified field equations (2.35) and (2.36) in a dust-dominated Universe ($p = 0$), we find that the static Universe obtained by Einstein corresponds to

$$\rho = \frac{\Lambda}{4\pi G} \quad , \quad \frac{K}{a^2} = \Lambda \tag{2.38}$$

Since ρ is positive, we require that Λ is positive. This means that the static Universe is a closed one ($K = +1$) with a radius $a = 1/\sqrt{\Lambda}$. Equations (2.38) show that the energy density ρ is determined by Λ.
The requirement of a cosmological constant to achieve a static Universe can be understood by having a look at Newton's equation of motion

$$m\ddot{a} = -\frac{Gm}{a^2}\left(\frac{4\pi a^3 \rho}{3}\right) \tag{2.39}$$

$$\left(\frac{\ddot{a}}{a}\right) = -\frac{4\pi G}{3}\rho \tag{2.40}$$

Since gravity pulls the point particle toward the center of the sphere, we need a repulsive force to realize a situation in which a is constant. This corresponds to adding a cosmological constant term $\Lambda/3$ on the right hand side of Eq. (2.40).
The above description of the static Universe was abandoned with the discovery of redshift of the distant stars, but it is intriguing that such a cosmological constant would come back in the 1990's to explain the observed acceleration of the Universe.

2.2.1. The fine tuning problem

The cosmological constant suffers from a severe fine-tuning problem.
We require that Λ is of order of the square of the present value of the Hubble parameter H_0, in order to realize the cosmic acceleration today. So we have:

$$\Lambda \approx H_0^2 = (2.13h \times 10^{-42} GeV)^2 \tag{2.41}$$

This corresponds to an energy density ρ_Λ,

$$\rho_\Lambda = \frac{\Lambda M_{pl}^2}{8\pi} \approx 10^{-47} GeV^4 \tag{2.42}$$

We consider that the energy-density in (2.42) gets contributions from zero point quantum fluctuations of all the fields present in Nature. Considering a

scalar particle of mass m, it gives:

$$\rho_{vac} = \frac{1}{2}\int_0^\infty \frac{d^3\mathbf{k}}{(2\pi)^3}\sqrt{k^2+m^2} \tag{2.43}$$

in the units of $\hbar = c = 1$. The integral (2.43) exhibits an ultraviolet divergence and therefore needs to be cut-off in the ultraviolet:

$$\rho_{vac} = \frac{1}{2}\int_0^{k_{max}} \frac{4\pi k^2 dk}{(2\pi)^3}\sqrt{k^2+m^2} \approx \frac{k_{max}^4}{16\pi^2} \tag{2.44}$$

If we pick up $k_{max} = M_{pl}$, we find that the vacuum energy density in this case is estimated as

$$\rho_{vac} \approx 10^{74} GeV^4 \tag{2.45}$$

which is about 10^{121} orders of magnitude larger than the observed value given by Eq. (2.42). Even we take an energy scale of QCD for k_{max}, we obtain $\rho_{vac} \approx 10^{-3}$ GeV^4 which is still much larger than ρ_Λ.
So far, there are no completely satisfactory solutions to this problem.
A possibility is to consider supersymmetry, which posits that for each fermionic degree of freedom there is a matching bosonic degree of freedom, and vice-versa. The positive thing is that, while bosonic fields contribute a positive vacuum energy, for fermions the contribution is negative. Hence, if the degrees of freedom exactly match, the net vacuum energy sums up to zero. However, in the real world there is no evidence that supersymmetry exists, otherwise we should have observed, for instance, a supersymmetric scalar partner of the electron, the *selectron*, of the same mass while the present experimental lower bounds on the masses of the scalar partners is of order of $M_{susy} >$ O(100 GeV).
The breaking of supersymmetry introduces a non-vanishing vacuum energy of order of $r_{vac} \sim M_{susy}^4$, so it reintroduces the cosmological constant problem.

2.2.2. The coincidence problem

The second aspect of the cosmological constant problems is called the *cosmic coincidence problem.* It seems very strange that we find ourselves in an epoch $t = t_0$ where the cosmological constant density is of the same order of the matter energy density, i.e. $\rho_\Lambda(t = t_0) \cong \rho_m(t = t_0)$. In view of the rapidly decreasing value of $\rho_m(a) \sim a^{-3}$, it is quite puzzling to observe that its current value is precisely of the same order of magnitude as the vacuum energy density ρ_Λ which remains constant as the Universe expands.
It is convenient to define the *cosmic coincidence ratio* as:

$$r(a) = \frac{\rho_\Lambda(a)}{\rho_m(a)} \tag{2.46}$$

For $\Omega_{m,0} \cong 0.3$ and $\Omega_{\Lambda,0} \cong 0.7$ we have that $r_0 \cong 2.3$, which is of $O(1)$. However, in ΛCDM model, where ρ_Λ is constant and $\rho_m(a \to \infty)$ goes to zero, the ratio r grows as the expansion of the Universe.
So the fact that r_0= O(1) is regarded as a puzzle because it suggest that $t = t_0$ is a very special epoch of our Universe.

2.3. QUINTESSENCE

Quintessence is an ordinary scalar field ϕ with a potential $V(\phi)$ which interacts with all the other components only through the standard gravity [9, 10, 11]. The potential determines how the scalar field affects the expansion of the Universe. The action for this model is given by:

$$S = \int d^4x\sqrt{-g}\left[\frac{M_{pl}^2}{2}\mathcal{R} + \mathcal{L}_\phi\right] + S_M \tag{2.47}$$

where $\mathcal{L}_\phi = -\frac{1}{2}g^{\mu\nu}\partial_\mu\phi\partial_\nu\phi - V(\phi)$ is the scalar field Lagrangian, $M_{pl} \equiv (\sqrt{8\pi G})^{-1}$, $\mathcal{R}$ is the Ricci scalar and S_M is the matter action.
The contribution of the scalar field to the total stress-energy tensor is given by

$$T^\phi_{\mu\nu} = -\frac{2}{\sqrt{-g}}\frac{\partial S}{\partial g^{\mu\nu}} = \partial_\mu\phi\partial_\nu\phi - g^{\mu\nu}\left[\frac{1}{2}g^{\alpha\beta}\partial_\alpha\phi\partial_\beta\phi + V(\phi)\right] \tag{2.48}$$

In a flat Friedmann background, we can obtain the energy density ρ_ϕ and the pressure P_ϕ:

$$\rho_\phi = -T_0^{0(\phi)} = \frac{1}{2}\dot{\phi}^2 + V(\phi) \quad , \quad P_\phi = T_i^{i(\phi)} = \frac{1}{2}\dot{\phi}^2 - V(\phi) \tag{2.49}$$

The ratio between these two quantities gives the equation of state for the scalar field

$$w_\phi = \frac{P_\phi}{\rho_\phi} = \frac{\dot{\phi}^2 - 2V(\phi)}{\dot{\phi}^2 + 2V(\phi)} \tag{2.50}$$

The variation of the action with respect to $g_{\mu\nu}$ gives the Einstein equations:

$$R_{\mu\nu} - \frac{1}{2}g_{\mu\nu}R = 8\pi G(T^{(m)}_{\mu\nu} + T^{(\phi)}_{\mu\nu}) \tag{2.51}$$

where $T^{(m)}_{\mu\nu} = \rho_m u^\mu u^\nu$ is the matter energy-momentum tensor.
Since there is no coupling between ϕ and other fields, the energy-momentum tensors are conserved separately:

$$T^{\mu\nu}_{(\phi);\mu} = 0 \quad , \quad T^{\mu\nu}_{(m);\mu} = 0 \tag{2.52}$$

From Eqs. (2.51) and using (2.49), we can derive the Friedmann equations:

$$H^2 = \frac{1}{3M_{pl}^2}\left(\rho_\phi + \rho_m\right) = \frac{1}{3M_{pl}^2}\left(\frac{1}{2}\dot{\phi}^2 + V(\phi) + \rho_m\right) \tag{2.53}$$

$$\left(\frac{\ddot{a}}{a}\right) = -\frac{1}{6M_{pl}^2}(\rho_m + \rho_\phi + 3P_\phi) = -\frac{1}{6M_{pl}^2}\left(2\dot{\phi}^2 - 2V(\phi) + \rho_m\right) \tag{2.54}$$

The variation of the action (2.47) with respect to the scalar field ϕ gives

$$\ddot{\phi} + 3H\dot{\phi} + \frac{dV(\phi)}{d\phi} = 0 \tag{2.55}$$

From the equation of state (2.50), we note that $-1 \leq w_\phi \leq 1$. For a flat potential (slow-roll limit), we have that $\dot{\phi}^2 \ll V(\phi)$ and, from Eq. (2.50), it corresponds to $w_\phi \simeq -1$ so it reproduces the cosmological constant case in which $\rho =$ const. For a steep potential, we have that the condition $\dot{\phi}^2 \gg V(\phi)$ is always satisfied and the equation of state becomes $w_\phi \simeq 1$ from Eq. (2.50). In this case, the scalar field energy density evolves as $\rho_\phi \propto a^{-6}$ much faster than the background fluid energy density. In order to realize the late-time acceleration of our Universe, we require that $w_\phi < -1/3$ and, from (2.50), it implies that $\dot{\phi}^2 < V(\phi)$.
Scalar fields in cosmology are ubiquitous; both the cosmology of weakly coupled scalar fields and their theoretical motivations have been much studied since the advent of the idea of inflation. Only, this field has an energy density that survives during the inflation and come to dominate the entire energy density today. However, the definition of Quintessence is different from that an *inflaton* field: indeed, Quintessence doesn't need to partecipate to the inflationary phase, i.e. it may not to be the same field as the *inflaton*.
We also note that if the scalar field dominated early enough, it would suppress the growth of baryonic structures on small scales, because the Universe expands faster than the perturbations can collapse.
In the context of inflation, we define the slow-roll parameters in this way [12]:

$$\epsilon = \frac{M_{pl}^2}{2}\left(\frac{1}{V}\frac{dV}{d\phi}\right)^2 \quad , \quad \eta = M_{pl}^2\left(\frac{1}{V}\frac{d^2V}{d\phi^2}\right) \tag{2.56}$$

Inflation occurs when these slow-roll conditions $\epsilon \ll 1$ and $|\eta| \ll 1$, are satisfied. In the context of dark energy, these slow-roll conditions are not completely trusty, since there exists dark matter as well as dark energy.

However they still provide a good measure to check the existence of a solution with an accelerated expansion. If we define the slow-roll parameters (2.56) in terms of the time-derivatives of H such as $\epsilon = -\dot{H}/H^2$, this is a good tool to check the existence of an accelerated expansion since they implement the contributions of both dark energy and dark matter.
It is of interest to derive a scalar-field potential that gives rise to a power-law expansion:

$$a(t) \propto t^p \tag{2.57}$$

The accelerated expansion occurs for $p > 1$. From Eqs. (2.53) and (2.54), by putting $\rho_m = 0$, we obtain the relation $\dot{H} = -(1/2M_{pl}^2)\dot{\phi}^2$. Then we find that $V(\phi)$ and $\dot{\phi}$ can be expressed in terms of H and $\dot{H}$:

$$V(\phi) = 3H^2 M_{pl}^2 \left(1 + \frac{\dot{H}}{3H^2}\right), \tag{2.58}$$

$$\phi(t) = 2M_{pl}^2 \int dt \left[-\dot{H}\right]^{1/2} \tag{2.59}$$

Here we chose the positive sign of $\dot{\phi}$. Hence the potential giving the power-law expansion (2.57) corresponds to:

$$V(\phi) = V_0 \exp\left(-\sqrt{\frac{2}{p}}\frac{\phi}{M_{pl}}\right) \tag{2.60}$$

where V_0 is a constant. The field evolves as $\phi(t) \propto \ln(t)$. The above result shows that the exponential potential, that could be used for dark energy, implies that $p > 1$.
In addition to the fact that exponential potentials can give rise to an accelerated expansion, they possess cosmological *scaling solutions* [13, 14] in which the field energy density ρ_ϕ is proportional to the matter energy density ρ_m.
The above discussion shows that scalar-field potentials which are not steep compared to exponential potentials can lead to an accelerated expansion.
In fact the original *Quintessence models* [9, 11] are described by the power-law type potential

$$V(\phi) = \frac{M^{4+\alpha}}{\phi^\alpha} \tag{2.61}$$

where α is a positive number (it could actually also be negative [15]) and M is constant. Where does the fine tuning arise in these models? Recall that we need to match the energy density of the quintessence field to the current critical energy density, that is

$$\rho_\phi^{(0)} \approx M_{pl}^2 H_0^2 \approx 10^{-47} GeV^4 \tag{2.62}$$

The mass squared of the field ϕ is given by $m_\phi^2 = \frac{d^2V(\phi)}{d\phi^2} \approx \rho_\phi/\phi^2$ and the Hubble expansion rate is given by $H^2 \approx \rho_\phi/M_{pl}^2$. When m_ϕ^2 decreases to of order of H_0^2 [9, 11], the Universe enters into a tracking regime in which the energy density of the field ϕ catches up the background fluid. This shows that the field value at present is of order of the Planck mass $\phi_0 \sim M_{pl}$, which is typical of most of the quintessence models. Since $\rho_\phi^{(0)} \approx V(\phi_0)$, we obtain the mass scale:

$$M = (\rho_\phi^{(0)} M_{pl}^\alpha)^{\frac{1}{4+\alpha}} \tag{2.63}$$

This constraints the allowed combination of α and M to be $M = 1$ GeV for $\alpha = 2$ [16]. We can reach the same conclusion by observing that, in order to satisfy the slow-roll condition $|\eta| \lesssim 1$ (2.56), we have that:

$$|m_\phi^2| \lesssim V_0/M_{pl}^2 \simeq H_0^2, \tag{2.64}$$

which gives:

$$|m_\phi^2| \lesssim H_0^2 \approx 10^{-33} eV \tag{2.65}$$

Nevertheless a general problem we always have to treat is finding such quintessence potentials in particle physics.

2.3.1. Further problems of minimally coupled quintessence

The exchange of very light fields with mass given by (2.65), gives rise to forces of very long range, so we have to consider the direct interaction of the quintessence field ϕ to ordinary matter.
As discussed in [17], there is the possibility that ϕ can couple to standard model fields through interactions of the form:

$$\beta_i \frac{\phi}{M} \mathcal{L}_i \tag{2.66}$$

where β_i is a dimensionless coupling, $\mathcal{L}_i$ is any gauge-invariant dimension-four operator, such as $F_{\mu\nu}F^{\mu\nu}$ or $i\bar{\psi}\gamma^\mu D_\mu \psi$ and M is the energy scale. In absence of detailed knowledge about the structure of the theory at high energies, the couplings β_i are expected to be of order of unity.
This scalar force mediated by ϕ can lead to observable violations of the universality of the free fall, which are constrained by Eötvös-type experiments. We remember that a direct test of the Weak-Equivalence Principle (WEP) is the comparison of the acceleration of two laboratory-sized bodies of different composition in an external gravitational field. If the principle is violated,

then the accelerations of different bodies would differ [18, 19, 20].
The simplest way to quantify such possible violations of WEP in a form suitable for comparison with experiment is to suppose that for a body with inertial mass m_I, the gravitational mass m_G is no longer equal to m_I, so that in a gravitational field g, the acceleration is given by $m_I a = m_G g$.
Now the inertial mass of a typical laboratory body is made up of several types of mass-energy: rest energy, electromagnetic energy, weak-interaction energy, and so on. If one of these forms of energy contributes to m_G differently than it does to m_I, a violation of WEP would result. One could then write:

$$m_G = m_I + \sum_A \frac{\eta^A E^A}{c^2} \tag{2.67}$$

where E^A is the internal energy of the body generated by interaction A, η^A is a dimensionless parameter that measures the strength of the violation of WEP induced by that interaction, and c is the speed of light.
A measurement or limit on the fractional difference in acceleration between two bodies then yields a quantity called the *Eötvös-ratio* given by:

$$\eta \equiv 2\frac{|a_1 - a_2|}{|a_1 + a_2|} = \sum_A \eta^A \left(\frac{E_1^A}{m_1 c^2} - \frac{E_2^A}{m_2 c^2} \right) \tag{2.68}$$

where we drop the subscript I from the inertial masses. Thus, experimental limits on η place limits on the WEP-violation parameters η_A.
As discussed in [21], the differential acceleration of various test bodies, in the direction of the Sun, is less than 10^{-12} times the strength of gravity. Such limits can be translated into constraints on the dimensionless couplings β_i; for example, we could calculate the charge on a test body due to a coupling $\beta_{G^2}(\phi/M)\mathrm{Tr}(G_{\mu\nu}G^{\mu\nu})$, where $G_{\mu\nu}$ is the field strength tensor for QCD [22]. From the results found by [21], is possible to put an upper limit on the coupling β_{G^2}:

$$|\beta_{G^2}| \leq 10^{-4} \left(\frac{M}{M_{pl}} \right) \tag{2.69}$$

Another important phenomenon is the time variation of the constants of nature [20].
Since the scalar field must be of order of M_{pl} over cosmological timescales $t_0 \sim H_0^{-1}$, a coupling such as $\beta_{F^2}(\phi/M)F_{\mu\nu}F^{\mu\nu}$ will lead to evolution of the fine-structure constant α. Various observations constrain such variation. For example, isotropic abundances in the Oklo natural reactor imply that $|\dot{\alpha}/\alpha| < 10^{-15}$ yr^{-1} over the past two billion years [23], and this lead to the

constrain:

$$|\beta_{F^2}| \leq 10^{-6} \left(\frac{MH_0}{\langle \dot{\phi} \rangle} \right) \tag{2.70}$$

where $\langle \dot{\phi} \rangle$ is the average rate of change in the last two billion years.
So, there is clearly a good evidence against the existence of a nearly-massless scalar fields coupled to the standard model via non-renormalizable interactions with strength of order $1/M_{pl}$ because they are incompatible with phenomenological constraints in the laboratory or in the solar system.
Therefore, in order to be viable, the effect of these cosmological scalar fields should be screened in the local environment, as discussed in [24].
An example of such *screening mechanisms* is at work in the *chameleon* models, discussed in [25, 26]. In this scenario the matter-scalar coupling induces an environment-dependent mass for the scalar field, which becomes extremely massive when or where matter density is high.
The *Vainshtein mechanism* [27, 28], operates when the scalar has derivative self- couplings which become important near matter sources such as the Earth. The strong coupling essentially cranks up the kinetic terms, which translates into a weakened matter coupling. Thus the scalar screens itself and becomes invisible to experiments. This mechanism is central to the phenomenological viability of braneworld modifications of gravity and galileon scalar theories [29, 30].
The last mechanism, the one explored in this thesis, is best known in the literature as the *symmetron mechanism* [31, 32, 33]. In its simplest implementation, a discrete symmetry is imposed on the scalar field. As a consequence, the matter-scalar coupling is non-vanishing only if the discrete symmetry is spontaneously broken, which happens when the environmental matter density drops below a critical value.

Chapter 3

The Symmetron Model

3.1. The Action

The symmetron model [31, 32, 33] can be introduced as a particular scalar-tensor theory, described by the action

$$S = \int d^4x\sqrt{-g}\left[\frac{M_{pl}^2}{2}\mathcal{R} - \frac{1}{2}\left(\partial\phi\right)^2 - V\left(\phi^2\right)\right] + \int d^4x\sqrt{-\tilde{g}}\,\mathcal{L}_m\left(\psi, \tilde{g}_{\mu\nu}\right)\,, \tag{3.1}$$

where

$$\tilde{g}_{\mu\nu} \equiv A^2\left(\phi^2\right) g_{\mu\nu}\,, \tag{3.2}$$

and by a Z_2 ($\phi \leftrightarrow -\phi$) symmetry imposed on the two functions V (scalar potential) and A (conformal matter-scalar coupling), which therefore can depend only on integer powers of ϕ^2. $\mathcal{R}$ is the Ricci scalar built from $g_{\mu\nu}$ and $M_{pl} \equiv (\sqrt{8\pi G})^{-1}$, where G is the Newton's constant in the Einstein frame and $\mathcal{L}_m$ is the matter lagrangian.
Eq. (3.2) relates the Einstein frame metric $g_{\mu\nu}$ to the Jordan frame one, $\tilde{g}_{\mu\nu}$. Since ϕ couples universally to all matter fields, the weak equivalence principle holds. Varying the action with respect to the scalar field, we obtain the field equations for ϕ:

$$\Box\phi - \frac{\partial V}{\partial\phi} - A^3\frac{\partial A}{\partial\phi}\tilde{T} = 0\,, \tag{3.3}$$

where $\tilde{T} = \tilde{g}_{\mu\nu}\tilde{T}^{\mu\nu}$ is the trace of the Jordan frame energy-momentum tensor $\tilde{T}_{\mu\nu} = -\left(2/\sqrt{-\tilde{g}}\right)\delta\mathcal{L}_m/\delta\tilde{g}^{\mu\nu}$ which is covariantly conserved with respect to $\tilde{g}_{\mu\nu}$: $\tilde{\nabla}_\mu\tilde{T}^\mu_\nu = 0$.
The Einstein equations are:

$$M_{pl}^2 G_{\mu\nu} = T^\phi_{\mu\nu} + A^2(\phi)\tilde{T}_{\mu\nu} \tag{3.4}$$

Since ϕ couples conformally to matter, its stress-energy tensor, which is given by:

$$T^{\phi}_{\mu\nu} = \partial_\mu\phi\partial_\nu\phi - \frac{1}{2}g_{\mu\nu}(\partial\phi)^2 - g_{\mu\nu}V(\phi) \tag{3.5}$$

is not covariantly conserved: $\nabla^\mu T^{\phi}_{\mu\nu} \neq 0$.
For astrophysical objects, we may use the idealization of pressureless sources, so $\tilde{T} \simeq -\tilde{\rho}$. Written in terms of the density $\rho = A^3\tilde{\rho}$, which is conserved in the Einstein frame, the scalar field equation (3.3) takes the form:

$$\Box\phi = \frac{\partial V}{\partial\phi} + \rho\frac{\partial A}{\partial\phi}\,. \tag{3.6}$$

Therefore, the field evolves according to an effective potential

$$V_{eff}\left(\phi^2\right) = V\left(\phi^2\right) + \rho A\left(\phi^2\right)\,. \tag{3.7}$$

As we said before, the functions $A(\phi^2)$ and $V(\phi^2)$ are assumed symmetric under $(\phi \leftrightarrow -\phi)$ and they are such that the effective symmetry breaking potential (3.7) has a zero vacuum expectation value (VEV) for large ρ and a large VEV for small ρ. In addition, the function $A(\phi^2)$ should be such that the coupling of scalar fluctuations $\delta\phi$ to matter is proportional to the VEV. The simplest symmetron theory, studied in [33], is described by these two functions:

$$V(\phi^2) = -\frac{1}{2}\mu^2\phi^2 + \frac{1}{4}\lambda\phi^4 \quad , \quad A(\phi^2) = 1 + \frac{1}{2M^2}\phi^2 + O\left(\frac{\phi^4}{M^4}\right) \tag{3.8}$$

where μ and M are two mass scales and λ is a dimensionless coupling constant.
In our model [34], we have chosen in this way the explicit forms for $V(\phi^2)$ and $A(\phi^2)$:

$$V\left(\phi^2\right) = \bar{V} + V_0\, e^{-\frac{\phi^2}{2M^2}}\,, \tag{3.9}$$

$$A\left(\phi^2\right) = e^{\frac{\lambda\phi^2}{2M^2}} \tag{3.10}$$

where $\bar{V}$ plays the role of a cosmological constant, V_0 is a energy density which will turn out to be $\ll \bar{V}$, λ is a dimensionless coupling constant (which will turn out to be $\ll 1$) and M is a new mass scale [31].
Our results will not change qualitatively if a functional form different from exponential would be chosen for the functions $V(\phi^2)$ and $A(\phi^2)$. Indeed, the phenomenological constraints reviewed in the next section imply that $\lambda,\ V_0/\bar{V} < O(10^{-9})$ and $\phi/M = O(1)$, so we can safely expand A to linear

order in ϕ^2 and consider a potential for V containing up to quadratic terms in ϕ^2. In this case, a new parameter (the coefficient of ϕ^4 in $V(\phi)$) would appear.

Assuming $\lambda > 0$, the effective potential V_{eff} induces a density-dependent phase transition. Indeed, its second derivative in $\phi = 0$ is given by

$$\left.\frac{d^2 V_{eff}}{d\phi^2}\right|_{\phi=0} = -V_0 + \lambda\rho\,, \tag{3.11}$$

which changes sign at a redshift z_t, given by.

$$\rho(z_t) = \rho_0(1+z_t)^3 = \frac{V_0}{\lambda}\,. \tag{3.12}$$

For $z \geq z_t$ the minimum of V_{eff} is at $\phi = 0$ and the discrete symmetry is restored, whereas for $z \leq z_t$ two degenerate minima form at the z-dependent values

$$\phi_{min}(z) = \pm M \left[\frac{6}{1+\lambda}\log\left(\frac{1+z_t}{1+z}\right)\right]^{1/2} \qquad (\text{for} \quad z \leq z_t) \tag{3.13}$$

and the discrete symmetry is spontaneously broken.
The coupling to matter is measured by the field-dependent quantity

$$\beta(\phi) = M_{Pl}\frac{d\log A\left(\phi^2\right)}{d\phi} = \lambda\frac{\phi M_{Pl}}{M^2}\,, \tag{3.14}$$

which, if evaluated at the z-dependent minimum, vanishes for $z \geq z_t$. At $z = 0$ it is given by

$$\beta_0 \equiv \beta(\phi_{min}(z=0)) = \lambda\frac{M_{Pl}}{M}\left[\frac{6}{1+\lambda}\log\left(1+z_t\right)\right]^{1/2}\,, \tag{3.15}$$

where we have chosen the minimum with the " + " sign in (3.13). Notice that, with respect to the dark sector of the ΛCDM, the model presents three extra parameters: indeed, besides $\bar{V}$ and ρ_0, playing the roles of ρ_Λ and ρ_m, respectively, we have the coupling λ, the constant V_0, and the new mass scale M. We decide to trade the latter for the more physically transparent parameters z_t, β_0, and $\mu \equiv M/M_{Pl}$. In the following, we will discuss the observational constraints on these parameters.

3.2. Screening mechanism

3.2.1. Static solutions

To study the constraints on the model from tests of gravity, we consider the symmetron profile around an astrophysical source. We model the latter by a sphere of radius R and homogeneous mass density ρ, whereas the background energy density is given by $\bar{\rho}$. The scalar field equation (3.3) in spherical coordinates, and in the static limit, reduces to

$$\frac{d^2\phi}{dr^2} + \frac{2}{r}\frac{d\phi}{dr} = V_{,\phi} + \rho A_{,\phi}\,. \tag{3.16}$$

Analogously to what is done in [33], the radial field equation can be thought of as fictional particle rolling in a potential $-V_{eff}$, subject to the friction term $\frac{2}{r}\frac{d\phi}{dr}$. The solutions of the scalar field inside and outside the object were found in [33]. They depend on a dimensionless parameter γ, called *thin-shell* parameter, defined as

$$\gamma \equiv \frac{\lambda}{M^2}\left(\rho\left(t\right) - \bar{\rho}\left(t\right)\right)R^2 = 6\,\lambda\,\frac{M_{Pl}^2}{M^2}\Phi\,, \tag{3.17}$$

where ρ is the matter density inside the sphere, $\bar{\rho}$ is the cosmological one, and Φ the gravitational potential of the spherical overdensity with respect to the cosmological background. Physically, this ratio measures the surface Newtonian potential relative to $M^2/\lambda M_{Pl}^2$. γ will soon be interpreted as a *thin-shell* factor for the solutions, in analogy with Chameleon models [25]. Indeed, (3.17) matches the chameleon *thin-shell* expression, therefore, symmetrons and chameleons have similar phenomenology, in particular for astrophysical tests. If we rewrite the density inside the sphere as

$$\rho\left(t\right) = \rho_i\left(\frac{R_i}{R\left(t\right)}\right)^3\,,$$

where ρ_i and R_i are respectively the initial density and the initial radius of the sphere, and the density of the background as

$$\bar{\rho}\left(t\right) = \bar{\rho}_i\left(\frac{a_i}{a\left(t\right)}\right)^3\,,$$

where $\bar{\rho}_i$ is the initial density of the background, the γ parameter becomes:

$$\gamma\left(t\right) = \frac{\lambda}{\mu^2}3H_0^2R_i^2\left[\left(1+\delta_{m,i}\right)\left(\frac{R_i}{R\left(t\right)}\right) - \left(\frac{a_i}{a\left(t\right)}\right)^3\left(\frac{R\left(t\right)}{R_i}\right)^2\right]\,, \tag{3.18}$$

where $\delta_{m,i}$ is the initial density contrast, defined as $\delta_{m,i} = \frac{\delta\rho_i}{\bar{\rho}_i} = \frac{\rho_i - \bar{\rho}_i}{\bar{\rho}_i}$.

Consider a test particle at a distance $R \ll r \ll m_\phi^{-1}$ away from the object, where m_ϕ is the mass of the scalar field. The scalar force to gravity ratio on this particle is [35]

$$\frac{F_\phi}{F_N} = -\frac{\beta(\phi)}{M_{Pl}} \frac{d\phi/dr}{F_N}\,, \tag{3.19}$$

with $\beta(\phi)$ given in (3.14). Substituting the expression for the scalar field outside the object ($r > R$) into Eq. (3.19), we have

$$\frac{F_\phi}{F_N} = 6\frac{\beta(\phi)^2}{\gamma}\left[1 - \sqrt{1/\gamma}\tanh\left(\sqrt{\gamma}\right)\right]\,, \tag{3.20}$$

from which the dependence of the fifth force on the parameter γ is manifest. Different astrophysical objects (stars, planets, galaxies) can be *screened* or *unscreened* according to their respective values for γ. If $\gamma \gg 1$, Eq. (3.20) reduces to [35]

$$\frac{F_\phi}{F_N} \simeq 6\frac{\beta(\phi)^2}{\gamma} \ll 1\,, \tag{3.21}$$

and the object is screened. In this regime the field inside the object is exponentially suppressed with respect to the asymptotical value outside, except within a *thin-shell* beneath the surface. In the opposite regime, $\gamma \ll 1$, we can Taylor expand Eq. (3.20), which gives [33]

$$\frac{F_\phi}{F_N} \simeq 2\beta^2 \tag{3.22}$$

There is no *thin-shell* in this case; the scalar field has basically the same value inside and outside the object, hence the symmetron couples with gravitational strength to the entire source.

3.3. Constraints from tests of gravity

Since the field is long ranged (and universally coupled) in almost all situations today the theory is best constrained by solar system experiments which have been performed with high precision.
In this section, we adapt the findings of [33] to the present implementation of the symmetron scenario. Requiring that our Galaxy is sufficiently screened, namely, that $\gamma_G > 10$, gives (from Eq. 3.17 and using $\Phi_G \sim 10^{-6}$)

$$\frac{M}{M_{Pl}} = \mu < \sqrt{\lambda\,\Phi_G} \lesssim 10^{-3}\lambda^{1/2}\,. \tag{3.23}$$

In this parameter regime, the Sun ($\Phi_\odot \sim 10^{-6}$) is also screened, but the Earth ($\Phi_\oplus \sim 10^{-9}$) is not [33].
GR tests in the solar system give constraints on the two post-Newtonian parameters, γ_{PPN} and β_{PPN} [20], which can be expressed in terms of the scalar coupling $\beta(\phi)$ of Eq. (3.14). The tightest constraint on γ_{PPN} comes from time-delay and light-deflection observations. In the present model, they imply

$$|\gamma_{PPN} - 1| = 2\frac{\beta(\phi)^2}{1+\beta(\phi)^2} \approx 2\lambda^2\phi^2\frac{M_{Pl}^2}{M^4} = \frac{1}{3}\gamma\frac{\phi^2}{M^2}\frac{\lambda}{\Phi}\,, \tag{3.24}$$

where, to obtain the last equality, we have used Eq. (3.17).
Near the Sun, using the solution of the field equation for the screened case [33], we have that $\phi = \phi_\odot \approx \phi_G/\sqrt{\gamma_\odot}$ where ϕ_G is the asymptotic value of ϕ inside the galaxy. The relation between ϕ_G and the asymptotic cosmological value today, $\bar{\phi}_0$, is also obtained from the solution of the field equation,

$$\sqrt{\gamma_\odot}\frac{\phi_\odot}{M} \simeq \frac{\phi_G}{M} \simeq \frac{\bar{\phi}_0}{M}\frac{R_G}{R_{s.s.}}\frac{1}{\sqrt{\gamma_G}}e^{\sqrt{\gamma_G}\left(1-\frac{R_{s.s}}{R_G}\right)} \simeq 3\cdot 10^{-2}\,\frac{\bar{\phi}_0}{M}\,, \tag{3.25}$$

where $R_G \sim 100\,\mathrm{kpc}$ is the galactic radius, $R_{s.s.} \sim 10\,\mathrm{kpc}$ is the distance between the solar system and the galactic center and, following [33], we have adopted the fiducial value $\gamma_G = 20$. Inserting (3.25) in (3.24) we have

$$|\gamma_{PPN} - 1| \simeq 3\cdot 10^4\lambda\left(\frac{\bar{\phi}_0}{M}\right)^2\,, \tag{3.26}$$

where we have also used $\Phi_\odot \sim 10^{-6}$. Since from (3.13) we have $\bar{\phi}_0/M = O(1)$, the current constraints from the Cassini spacecraft [36], $|\gamma_{PPN} - 1| \approx 10^{-5}$ can be satisfied for $\lambda \lesssim 10^{-9}$. Similar bounds come from the Nordvedt Effect, which describes the difference in free-fall acceleration of the Moon and the Earth towards the Sun due to scalar-induced differences in their gravitational binding energy.
Finally, constraints from binary pulsars are trivially satisfied, since both the neutron star and its companion are screened. As we can see from [33], the force between these bodies is therefore suppressed by two *thin-shell* factors:

$$\frac{F_\phi}{F_N} = \frac{1}{\gamma_{pulsar}}\cdot\frac{1}{\gamma_{companion}}\,. \tag{3.27}$$

Estimating $\Phi_{pulsar} \sim 0.1$ and $\Phi_{companion} \sim 10^{-6}$, then for our fiducial parameter choices we obtain $\gamma_{pulsar} \sim 10^5$, $\gamma_{companion} \sim 10$ and therefore $\frac{F_\phi}{F_N} \approx 10^{-6}$, well below the current pulsar constraints on scalar-tensor theories.

The scalar field mass in the cosmological background is given by the second derivative of the effective potential (3.7) evaluated in $\bar{\phi}_0$. It is

$$m_\phi^2 \sim \frac{V_0}{M^2} \sim \frac{\lambda}{\mu^2}\frac{\rho_0}{M_{Pl}^2} > 10^6 H_0^2\,, \tag{3.28}$$

where we have used eqs. (3.12) and (3.23). This is in agreement with the findings of refs. [37, 38] and implies that the scalar field range is smaller than $O(\text{Mpc})$, and therefore the scalar force gives no observable signature on linear and mildly non-linear scales, which are above $O(10\text{ Mpc})$.
In the next sections we will discuss the effect of the symmetron model on non-linear scales, by using the spherical collapse approximation.

Chapter 4

Non-linear evolution of cosmological perturbations

An interesting point of view is the study of the growth of density perturbations during a regime which lies between the linear perturbation theory and the full non-linear dynamics that can be treat only with N-body simulations. To do this, we can perform a semi-analytic study by using the *spherical collapse model* in order to provide a complementary physical insight on what is going on respect to the previous results obtained from N-body simulations that have been performed for Chameleon [39], Vainshtein [40], and Symmetron [41, 42] models. In this chapter, we'll study the symmetron model in the spherical collapse approximation and then we'll use the outputs of this analysis to compute the halo mass function and the linear bias.

4.1. Spherical collapse

A standard approach to follow the evolution of cold dark matter structures during the first stages of the non-linear regime is the spherical collapse model [43, 44, 45]. This approach was first applied to the EdS Universe and later on in the context of the ΛCDM [46]. Recently, the spherical collapse approximation has been also extended to quintessence models, as for instance in [47, 48].
In the following we will briefly review the basic equations in the EdS and ΛCDM cases and then we will extend these to the symmetron model.

4.1.1. Application to standard cosmologies

Consider a spherical density perturbation of radius R within a homogeneous background Universe. Under the effect of the gravitational attraction, the perturbation grows, possibly entering the nonlinear regime, depending on the scale of the perturbation. As a consequence of Birkhoff's theorem we can treat the spherical overdensity as a closed Universe where the total density $\rho = \bar{\rho} + \delta\rho$ exceeds the density of the background $\bar{\rho}$ due to the presence of the density perturbation. The radius R evolves according to the Friedmann equation:

$$\frac{\ddot{R}}{R} = -\frac{1}{6M_{Pl}^2}\sum_\alpha \rho_\alpha \left[(1+3w_\alpha)\right] \tag{4.1}$$

where the sum is over particle species. This sphere is embedded in a homogeneous Friedmann-Robertson-Walker (FRW) background characterized by the scale factor $a(t)$ and the Hubble function $\bar{H} \equiv \dot{a}/a$. We use a bar to indicate background quantities. With this notation the Friedmann equations describing the homogeneous and flat background Universe are:

$$\bar{H}^2 = \frac{1}{3M_{Pl}^2}\sum_\alpha \bar{\rho}_\alpha \tag{4.2}$$

$$\left(\frac{\ddot{a}}{a}\right) = -\frac{1}{6M_{Pl}^2}\sum_\alpha \bar{\rho}_\alpha \left[(1+3\bar{w}_\alpha)\right] . \tag{4.3}$$

In the EdS and ΛCDM scenarios, the matter energy density ρ_m and the cosmological constant energy density ρ_Λ are conserved, both inside and outside the spherical perturbation:

$$\dot{\rho}_m + 3H\rho_m = 0 \tag{4.4}$$

$$\dot{\bar{\rho}}_m + 3\bar{H}\bar{\rho}_m = 0 \tag{4.5}$$

$$\bar{\rho}_\Lambda = \rho_\Lambda = \text{const.} \tag{4.6}$$

The non-linear density contrast is defined by $1 + \delta_m \equiv \rho_m/\bar{\rho}_m$ and it is determined by Eqs. (4.4) and (4.5). Linear perturbation theory [49], on the other hand, gives the evolution equation:

$$\ddot{\delta}_{m,L} + 2\bar{H}\dot{\delta}_{m,L} - \frac{1}{2M_{Pl}^2}\bar{\rho}_m\delta_{m,L} = 0 . \tag{4.7}$$

Eqs. (4.1)–(4.7) can be integrated numerically. We start the integration at some initial time t_{in} when the total energy density in the spherical overdensity is higher than the critical energy density, due to the presence of the

perturbation δ_m. Eq. (4.1) gives the function $R(z)$. This first increases as the spherical perturbation expands following the background evolution, then it reaches a maximum value (turnaround) in which comoving velocities become zero; finally, the sphere collapses and its radius tends to zero. The redshift of collapse depends on the initial density contrast $\delta_{m,i}$: the higher is $\delta_{m,i}$, the earlier the overdense region collapses. The corresponding value of the linear density contrast extrapolated at the time of collapse is referred to as δ_c and it can be calculated by stopping the evolution of Eq. (4.7) when δ_m goes to infinity, i.e. the overdensity collapses. Varying the initial conditions one obtains different collapse redshifts z_c. In this way we derive the redshift dependence of the critical density $\delta_c = \delta_c(z_c)$. To be sure of starting the integration when overdensities are still linear, we find that it is necessary to work in a range of initial overdensities with $\delta_{m,in} \ll 1$ (in our numerical computations, we take $\delta_{m,in} \lesssim 10^{-3}$) . The quantity δ_c is important because it represents one of the key ingredients to calculate the halo-mass function, which provides a statistical information on the mass distribution of the collapsed spherical overdensities, *i.e.* the dark matter halos (see sect. 5).
In an EdS scenario the linear density contrast at collapse can be calculated analytically [44, 45] and it is equal to a constant value independent of the redshift of collapse z_c:

$$\delta_c = (3/20)\,(12\pi)^{2/3} \simeq 1.686\,. \tag{4.8}$$

In the ΛCDM case, instead, this value decreases for late collapse times, when dark energy dominates over matter and leads to cosmic acceleration, slowing down the structure formation. This well known effect is shown in Fig. 6.2, where we plot $\delta_c(z_c)$ for the EdS and the ΛCDM scenarios.

4.1.2. Application to the symmetron model

Now we generalize the spherical collapse equations to the case of the symmetron model. We make here a few simplifying assumptions which nevertheless allow us to properly account for the main features of the symmetron mediated force. We approximate the coupling function $\beta(\phi)$ inside the spherical overdensity to be equal to the cosmological one, $\beta(\phi_{min}(z))$, as long as the parameter γ, computed according to eq. (3.18), is smaller than a threshold value $\gamma_{tr} = \mathcal{O}(1)$, and to drop to zero everywhere inside the overdensity as soon as $\gamma > \gamma_{tr}$ (for a refined treatment of the scale dependence of the coupling $\beta(\phi)$ and of the overdensity profile, see ref. [50]). Moreover, we consider only spherical overdensities characterized by $m_\phi R < 1$, a requirement which considerably simplifies the Poisson equation for the scalar field fluctuations.

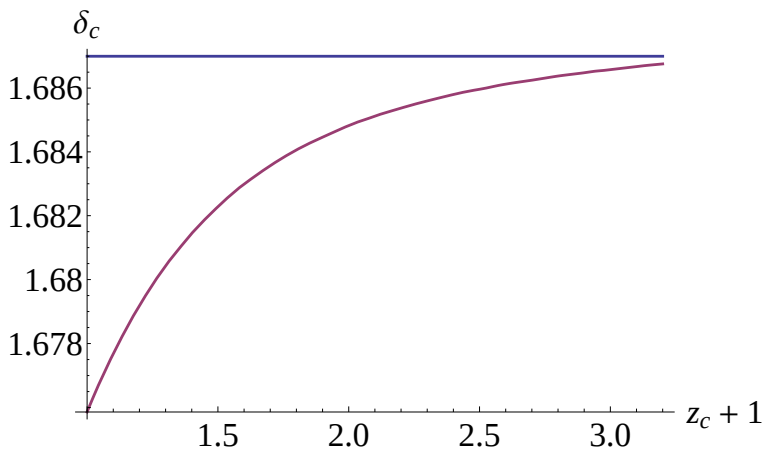

Figure 4.1: Extrapolated linear density contrast at collapse δ_c vs. $z_c + 1$ for EdS (blue curve) and ΛCDM (red curve) models.

Within these assumptions we can treat the evolution of the sphere of radius R as the one of a closed Universe coupled to the background expansion.

We start with a qualitative description of the spherical collapse in the symmetron model. In general, before the phase transition ($z > z_t$) the symmetron sits on the minimum $\phi = \phi_{min} = 0$ and the model coincides with the ΛCDM. After the phase transition ($z < z_t$), the symmetron evolves towards a different minimum $\phi = \phi_{min} \neq 0$ (3.13) which implies $\beta(\phi) \neq 0$ and therefore a spherical collapse potentially different from the one of the ΛCDM. Let us now assume $\beta(\phi) \neq 0$. Initially, for all the time before the phase transition, the scalar field is zero inside the sphere and in the background, so is not important to clarify if the sphere is in the thick-shell or in the thin-shell regime; only after the phase transition, the subsequent evolution of the sphere will always drive the γ parameter towards values larger than the $\mathcal{O}(1)$ threshold γ_{tr}, independently from the initial radius R_i of the overdensity, as one can see taking the limit $R \to 0$ in Eq. (3.17). In practice, however, dark matter halos form at the virialization radius $R = R_{vir}$, corresponding to a value of γ which we denote here by γ_{vir}. This allows us to clearly identify two different scenarios: for small enough initial radii the overdensity viarializes when $\gamma_{vir} < \gamma_{tr}$, and therefore the sphere remains in the thick-shell regime until the associated dark matter halo has formed. For large initial radii, instead, dark matter halos form when $\gamma_{vir} > \gamma_{tr}$, which implies a transition from the thick-shell regime to the *thin-shell* regime, defined in fact by the condition $\gamma > \gamma_{tr}$.

We now introduce the equations which quantitatively describe the spher-

ical collapse in the symmetron model. We denote by ϕ the scalar field inside the sphere and by $\bar{\phi}$ the background scalar field.
The flat background Universe is described by the Friedmann equations:

$$\frac{\ddot{a}}{a} = -\frac{1}{6M_{Pl}^2}\left[\bar{\rho}_m A\left(\bar{\phi}^2\right) + \bar{\rho}_\phi + 3\bar{p}_\phi\right] \tag{4.9}$$

$$\left(\frac{\dot{a}}{a}\right)^2 = \frac{1}{3M_{Pl}^2}\left[\bar{\rho}_m A\left(\bar{\phi}^2\right) + \bar{\rho}_\phi\right] \tag{4.10}$$

where

$$\bar{\rho}_\phi = \frac{1}{2}\dot{\bar{\phi}}^2 + V\left(\bar{\phi}^2\right) \tag{4.11}$$

$$\bar{p}_\phi = \frac{1}{2}\dot{\bar{\phi}}^2 - V\left(\bar{\phi}^2\right) \tag{4.12}$$

are respectively the density and the pressure of the background scalar field. We can derive the evolution equation for the sphere radius R by following the same steps of [48]. We find:

$$\frac{\ddot{R}}{R} = -\beta\left(\phi\right)\dot{\bar{\phi}}\left(\bar{H} - \frac{\dot{R}}{R}\right) + \frac{\ddot{a}}{a} - \frac{1}{6M_{Pl}^2}\bar{\rho}_m\delta_m\left[1 + 2\beta\left(\phi\right)^2\right] . \tag{4.13}$$

This equation describes the general evolution of the radius of a spherical overdense region subject to a scalar coupling $\beta(\phi)$, which controls the terms responsible for the additional attractive force. Since the scalar field slowly evolves following the background minimum $\phi_{min}(z)$, we can safely neglect all terms proportional to $\dot{\bar{\phi}}$ in Eq. (4.9), (4.10) and (4.13). This leads to:

$$\frac{\ddot{a}}{a} = -\frac{1}{6M_{Pl}^2}\left[\bar{\rho}_m A\left(\bar{\phi}^2\right) - 2V\left(\bar{\phi}^2\right)\right] \tag{4.14}$$

$$\left(\frac{\dot{a}}{a}\right)^2 = \frac{1}{3M_{Pl}^2}\left[\bar{\rho}_m A\left(\bar{\phi}^2\right) + V\left(\bar{\phi}^2\right)\right] \tag{4.15}$$

$$\frac{\ddot{R}}{R} = \frac{\ddot{a}}{a} - \frac{1}{6M_{Pl}^2}\bar{\rho}_m\delta_m\left[1 + 2\beta(\phi)^2\right] . \tag{4.16}$$

We now present the results of a numerical integration of the equations for the spherical collapse in the symmetron model. In our examples, we will fix the scalar coupling today, defined in (3.15), at $\beta_0 = 1$, and we fix $z_t = 1$ and $\mu = 10^{-9}$. With these parameters, spherical overdensities of initial radii smaller than $0.9\ \mathrm{Mpc\,h^{-1}}$ in comoving units do not cross the $\gamma = 1$ threshold before virialization, therefore their evolution takes place entirely in the thick shell regime. If we integrate numerically Eqs. (4.14), (4.15) and (4.16) from

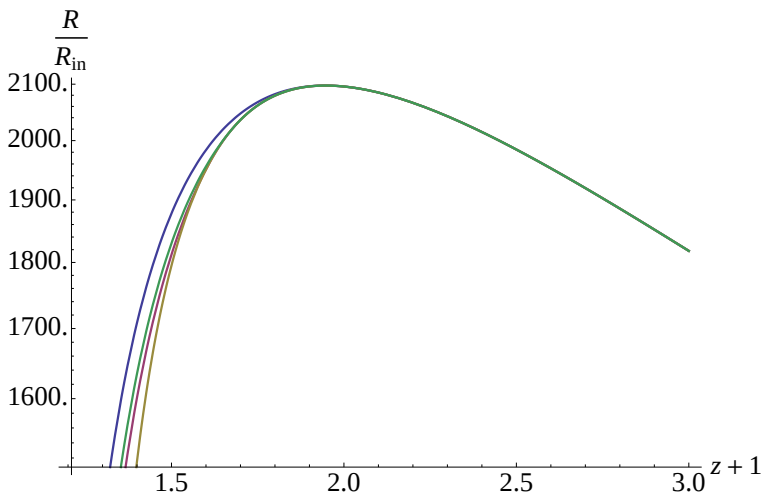

Figure 4.2: Evolution of radius $\frac{R}{R_i}$ vs redshift for $\delta_{m,i} = 0.0003$. The blu curve represents the ΛCDM model, the green curve and the red curve are associated with the transition regime from *thick* to *thin-shell* obtained by fixing $R_i \sim 4$ Mpc h^{-1} and $R_i \sim 3.5$ Mpc h^{-1} respectively and the yellow curve represents the *thick-shell* regime, obtained by fixing $R_i = 0.9$ Mpc h^{-1}. As we can see, before the phase transition ($z \geq 1$) the models coincide with the ΛCDM. After the phase transition ($z < 1$), we observe that the sphere collapses earlier in the *thick-shell* regime (yellow curve) with respect to the other models. We can also see that at $z \sim 0.6$ the yellow curve starts to be different from the red curve: this point represents the transition from *thick* to *thin-shell* and the moment in which γ becomes larger than γ_{tr}.

$z_i \sim 7000$ to $z_f = 0$, with an initial density contrast $\delta_{m,i} = 0.0003$ and setting $\phi(z) = \phi_{min}(z)$ at all z, we observe that the radius collapses at $z \simeq 0.3$, as we can see from Fig. 6.1.

For large initial radii, namely $R_i \gtrsim 0.9$ Mpc h^{-1}, the spherical collapse passes through a thick-shell/thin-shell transition before collapsing. After the transition the scalar force is confined only within a thin-shell beneath the surface so the sphere collapses later with respect to the case in which the object is unscreened, as one can see from Fig. 6.1.

Having determined the evolution of R in time, we can now determine δ_c. We follow the same steps of [48] to obtain the non-linear evolution of the

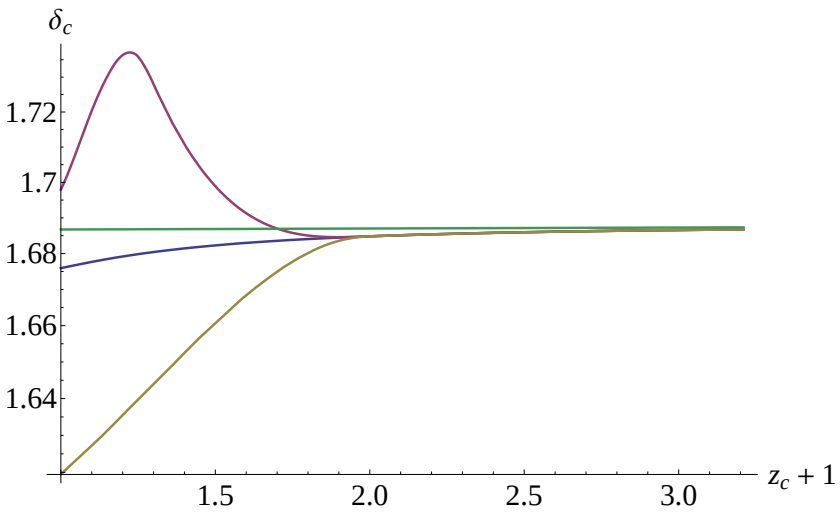

FIGURE 4.3: Extrapolated linear density contrast at collapse δ_c vs. $z_c + 1$ for EdS (green curve), ΛCDM (blue curve), transition from *thick* to *thin-shell* regime (red curve) and *thick-shell* regime (yellow curve) models.

density contrast:

$$\ddot{\delta}_m = \left(\beta\dot{\bar{\phi}} - 2\bar{H}\right)\dot{\delta}_m + \frac{4}{3}\frac{\dot{\delta}_m^2}{1+\delta_m} + \frac{1+\delta_m}{a^2}\nabla^2\Phi_{eff}\,. \tag{4.17}$$

Linearization leads to

$$\ddot{\delta}_{m,L} = \left(\beta\dot{\bar{\phi}} - 2\bar{H}\right)\dot{\delta}_{m,L} + \frac{1}{a^2}\nabla^2\Phi_{eff} \tag{4.18}$$

where Φ_{eff} is the effective gravitational potential given by

$$\Phi_{eff} \equiv \Phi + \beta\delta\phi \tag{4.19}$$

which obeys the modified Poisson equation

$$\nabla^2\Phi_{eff} = \frac{a^2}{2M_{Pl}^2}\bar{\rho}_m\delta_m\left(1+2\beta^2\right) \tag{4.20}$$

and Φ the usual gravitational potential. Since the scalar field is slowly varying during the spherical collapse, we can neglect all terms proportional to $\dot{\bar{\phi}}$ in Eq. (4.18) and write

$$\ddot{\delta}_{m,L} \simeq -2\bar{H}\dot{\delta}_{m,L} + \frac{1}{a^2}\nabla^2\Phi_{eff} \tag{4.21}$$

where $\bar{H}$ is defined in Eq. (4.2). When $\beta(\phi)$=0, Eq. (4.21) coincides with Eq. (4.7). We numerically solve Eq. (4.21) from $z_i \sim 7000$ to $z_f = 0$ and calculate the value of the linear density contrast at collapse $\delta_{m,L}(z = z_c)$ for different z_c by varying the value of $\delta_{m,i}$, as we have done for the ΛCDM case. From Fig. 4.3 one can see that the two scenarios studied here (*thick-shell* regime and transition from *thick* to *thin-shell* regime) approach the ΛCDM prediction at high redshifts corresponding to the Z_2-symmetric phase. At $z = 0$, the difference in δ_c with respect to the ΛCDM case is of about 2% for the *thin-shell* regime and of about 5% for the *thick-shell* regime, with the present choice of parameters.

4.2. Halo mass function and bias

The halo-mass function is defined as the comoving number density of halos per logarithmic interval in the virial mass M_v [44, 45]. Recently there has been a renewed theoretical interest regarding the halo mass function which has led to a variety of novel approaches to its determination, including interesting applications of the path integral formalism [51]. In the present analysis, which aims at comparing the predictions of our symmetron model with standard ΛCDM results, we will use a simple prescription for the halo mass function which relies on the Press-Schechter theory and on a scaling function first proposed by Sheth and Tormen (ST) [52]. This approach has been tested in various frameworks (see for instance [53]) and it guarantees sufficient accuracy for the purposes of the present work. Within these assumptions, the halo mass function takes the following form [52]

$$n_{\ln M_v} \equiv \frac{dn}{d\ln M_v} = \frac{\bar{\rho}_m A(\bar{\phi})}{M_v} f(\nu) \frac{d\nu}{d\ln M_v}, \tag{4.22}$$

where the linear power spectrum entering in the variable $\nu = \delta_c/\sigma(M_v)$ is evaluated at present time. Here $\sigma(M_v)$ is the variance of the linear density field convolved with a top hat of radius r that encloses the mass $M_v = 4\pi r^3 \bar{\rho}_m A(\bar{\phi})/3$, namely

$$\sigma^2(M) = \int \frac{d^3k}{(2\pi)^3} \left|\tilde{W}(kr)\right|^2 P_L(k), \tag{4.23}$$

where $P_L(k)$ is the linear power spectrum and $\tilde{W}$ is the Fourier transform of the top hat window function. The ST scaling function appearing in Eq. (4.22) is given by

$$\nu f(\nu) = \xi \sqrt{\frac{2}{\pi} a\nu^2} \left[1 + \left(a\nu^2\right)^{-p}\right] \exp\left[-a\nu^2/2\right], \tag{4.24}$$

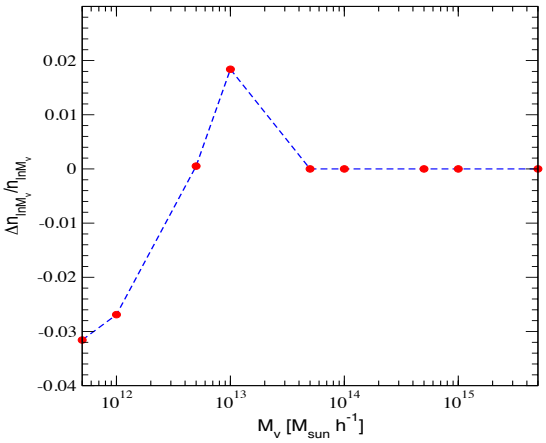

FIGURE 4.4: Relative deviation from the ΛCDM prediction of the halo mass function obtained within the symmetron model. The dependence of δ_c on the virial mass has been included as explained in the text. The red dots correspond to the masses for which we actually calculated the halo mass function, whereas the blue dashed curve connecting them has been drawn for illustrative purposes.

where the normalization constant ξ guarantees that f is correctly normalized, *i.e.* $\int d\nu f(\nu) = 1$. In all numerical applications of this expression presented here we will assume $p = 0.3$ and $a = 0.75$ [53].

Contrary to the ΛCDM case, in the symmetron model the calculation of the halo mass function is complicated by the fact that δ_c depends on the initial radius of the collapsing structure, and therefore in turn on its virial mass. To handle this complication within the ST approach we have calculated $\delta_c(z = 0)$ for a sample of virial masses spanning the mass range between $5 \times 10^{11} M_\odot\ h^{-1}$ and $5 \times 10^{15} M_\odot\ h^{-1}$, and than used these values of $\delta_c(z = 0)$ to evaluate the mass function. For each mass in this range we have used the appropriate value of δ_c. In Fig. 4.4 we show the halo mass function resulting from this procedure. Since the differences with respect to the ΛCDM case are at the few percent level, rather than showing the halo

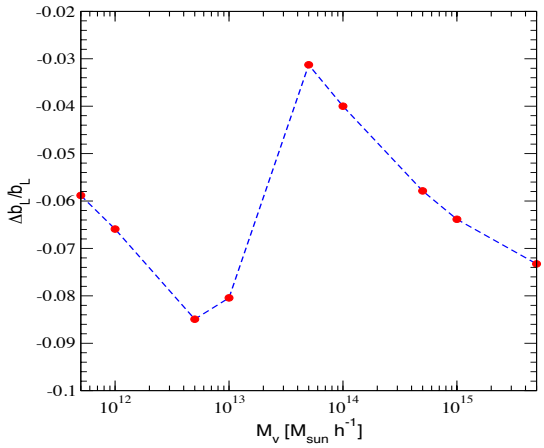

FIGURE 4.5: Relative deviation from the ΛCDM prediction of the linear bias of the symmetron model. Since b_L explicitly depends on δ_c (and not only through the variable ν), contrary to the case of the mass function, also at large virial masses we observe percent deviations of our model from the ΛCDM prediction.

mass function itself, we plot the relative difference between the halo mass function of the symmetron model and the corresponding quantity calculated for the ΛCDM. The red dots correspond to the masses for which we actually calculated the halo mass function, whereas the blue dashed curve connecting them has been drawn for illustrative purposes. As one can clearly see from this figure, for virial masses larger than about $10^{13} M_\odot\ h^{-1}$, the halo mass function of the symmetron model tends towards the one of the ΛCDM. The reason is that in the large virial mass limit the two models differ for their linear growth function only (as we can see from Fig. 6.1, if we increase the value of the initial radius, the sphere collapses at redshift closer to ΛCDM: for values of $R_i > 5$ Mpc h^{-1}, the sphere collapses at the same redshift of ΛCDM). This quantity cancels in the ratio which defines the variable ν, which thereby depends in both cases on the same initial conditions only.

We conclude this section focusing on the dark matter halo bias.

Collapsed dark matter halos are biased tracers of the underlying dark matter distribution. This bias can be quantified comparing the halo-mass cross power spectrum with the matter power spectrum. Within the ST framework the linear bias (*i.e.* the bias in the limit $k \to 0$) takes the following form [52]

$$b_L\left(M_v\right) = 1 + \frac{a\nu^2 - 1}{\delta_c} + \frac{2p}{\delta_c\left[1 + (a\nu^2)^p\right]} \,. \tag{4.25}$$

In Fig. 4.5 we show the predictions of our model and compare them with standard ΛCDM expectations. Also in the case of the linear bias we employ the same approach outlined above to account for the dependence of δ_c on the viral mass. Since b_L explicitly depends on δ_c (and not only through the variable ν), also at large virial masses we observe percent deviations of our model from the ΛCDM prediction. The feature in the plot at about $10^{13} M_\odot\, h^{-1}$ corresponds in fact to the transition between a regime where the variable ν coincides in the two scenarios to a regime in which ν is different in the two cases.

Chapter 5

Modified gravity theories

At the end of Chapter 1 we introduced cosmological models able to produce an accelerated expansion phase without a cosmological constant, so called *Quintessence models*. We can think of them as *Modified matter theories* since they are constructed modifying the right side of Einstein equations:

$$G_{\mu\nu} = 8\pi G T^{mod}_{\mu\nu} \tag{5.1}$$

In these models, the acceleration of the Universe is produced thanks to the introduction of new energy components besides matter and radiation in $T_{\mu\nu}$. Also the cosmological constant Λ can be seen as a modified matter theory since it can be introduced as an addition to the stress-energy tensor $T_{\mu\nu}$:

$$G_{\mu\nu} = 8\pi G T_{\mu\nu} + \Lambda g_{\mu\nu} \Rightarrow 8\pi G T^{mod}_{\mu\nu} \tag{5.2}$$

Nevertheless the cosmological constant can be also seen as a modification to Einstein's General Relativity Lagrangian, by introducing it at the left side of Einstein equations as a modification of the Einstein tensor $G_{\mu\nu}$. In general, another possible way to produce an accelerated expansion phase is to modify the gravity theory:

$$G^{mod}_{\mu\nu} = 8\pi G T_{\mu\nu} \tag{5.3}$$

This kind of theories that modify the Einstein tensor are known as *Modified gravity Theories*. We remember that the first modifications of General Relativity were made at the beginning of the twentieth century by Weyl [54] and Eddington [55] since they introduced higher order invariant terms in the Lagrangian.
Later on, attempts to build a quantum theory of gravity also lead to modification of GR. However, these modifications arise from quantum corrections which are important only at high energies and curvatures; from the cosmological point of view, it means that we are considering epochs close to the

Big Bang.
In order to generate the present cosmic acceleration of the Universe, the modifications have to be important when energy and curvature are low, contrary to the previous case.
One of the simplest ways to modify General Relativity is to replace the Ricci scalar R with a general function of itself $f(R)$ into the Lagrangian, without the introduction of other scalar quantities:

$$S = \frac{M_{pl}^2}{2} \int d^4x \sqrt{-g} f(R) + S_m(g_{\mu\nu}, \psi_m), \tag{5.4}$$

Theories with this kind of action are known as $f(R)$ *gravity theories* [56, 57].
Another class of modified gravity models is the one of *Scalar-Tensor theories* [58, 59, 60]; thanks to a proper coupling between the Ricci scalar R and a scalar field ϕ, these theories may produce the cosmic acceleration that we actually observe.
The general action for scalar-tensor theories can be written as :

$$S = \int d^4x \sqrt{-g} \left[\frac{M_{pl}^2}{2} f(\phi, R) - \frac{1}{2} \zeta(\phi) \left(\nabla\phi\right)^2 \right] + S_m(g_{\mu\nu}, \psi_m) \tag{5.5}$$

where f depends on the scalar field ϕ and on the Ricci scalar R, ζ is a function of ϕ and S_m is the matter Lagrangian that depends on the metric $g_{\mu\nu}$ and on matter fields ψ_m. The $f(R)$ gravity is a subclass of scalar-tensor theories since it corresponds to the choice: $f(\phi, R) = f(R)$ and $\zeta(\phi) = 0$. Also the Brans-Dicke theory is a particular example of scalar tensor theories, which corresponds to the choice: $f = \phi R$ and $\zeta = \omega_{BD}/\phi$, where ω_{BD} is the Brans-Dicke parameter. A generalization of the Brans-Dicke theory can be obtained by adding the potential $U(\phi)$ to the action (5.5), which correspond to the choice: $f = \phi R - 2U(\phi)$ and $\zeta = \omega_{BD}/\phi$.
We consider theories in which the function $f(\phi, R)$ takes the form:

$$f(\phi, R) = F(\phi)R - 2U(\phi) \tag{5.6}$$

where $F(\phi) \equiv \frac{\partial f}{\partial R}$. Then the action (5.5) in the Jordan frame becomes:

$$S = \int d^4x \sqrt{-g} \left[\frac{M_{pl}^2}{2} F(\varphi) R - \frac{1}{2}(1 - 6Q^2) F(\varphi) \left(\nabla\varphi\right)^2 - U(\varphi) \right] + S_m(g_{\mu\nu}, \psi_m) \tag{5.7}$$

where:

$$\varphi = \int d\phi \sqrt{\frac{3}{2} \left(\frac{F_{,\phi}}{F} \right)^2 + \frac{\zeta}{F}} \tag{5.8}$$

We also introduce the strength of the coupling between dark energy and matter, Q, which is given by:

$$Q \equiv -\frac{F_{,\varphi}}{2F} = -\frac{F_{,\phi}}{F}\left[\frac{3}{2}\left(\frac{F_{,\phi}}{F}\right)^2 + \frac{\zeta}{F}\right]^{-1/2} \tag{5.9}$$

If Q is constant, from Eq. (5.8) and (5.9) we have:

$$F = e^{-2Q\varphi} \tag{5.10}$$

and

$$\zeta = (1 - 6Q^2)F\left(\frac{d\varphi}{d\phi}\right)^2 \tag{5.11}$$

If we transform the action (5.7) from the Jordan frame to the Einstein frame through a conformal transformation $\tilde{g}_{\mu\nu} = F(\phi)g_{\mu\nu}$, we obtain an action equivalent to that used for the chameleon model [25, 26]. So the symmetron model discussed in the previous chapter can be considered as a modified gravity model since its action (Eq. (3.1)) is a particular case of the action for the chameleon model.
There is also another class of modified gravity models that is motivated by quantum gravity theories. In the braneworld models proposed by Dvali, Gabadadze and Porrati (DGP models) [29] the strong, weak and electromagnetic forces are confined into 4-dimensions, while gravity acts on 5 dimensions; for this kind of models, we require that Newton's gravity is recovered at small scales, while the effect of the fifth dimension is important at large scales leading to an acceleration of the Universe expansion, produced without the introduction of any additional components. The models based on $f(R)$ and on scalar-tensor theories can be compatible with local gravity constraints under the chameleon mechanism as long as the scalar degree of freedom has a large effective mass in the region of high density [25].
For the DGP model and also for the Galileon gravity model [30], the non-linear field self-interaction can allow to recover the General Relativistic behavior in the local region through the Vainshtein mechanism.
For the dark energy models mentioned so far, the field equations of motion are kept up to the second order. As shown by the Ostrogradski's theorem [61], this is a necessary (but not sufficient) condition to avoid the instabilities associated with the derivatives higher than the second order.
In 1974 Horndeski [62] derived the most general 4- dimensional single-field Lagrangian for scalar-tensor theories which gives second-order equations of motion; more recently, in connection to the covariant Galileon field, this theory was rediscovered by Deffayet et al. [63].

5.1. The Horndeski Lagrangian

The Horndeski Lagrangian (HL), which describes the dark energy sector, is given by the sum of four terms:

$$\mathcal{L} = \sum_{i=2}^{5} \mathcal{L}_i \tag{5.12}$$

where:

$$\begin{aligned}
\mathcal{L}_2 &= K(\phi, X), && (5.13)\\
\mathcal{L}_3 &= -G_3(\phi, X)\Box\phi, && (5.14)\\
\mathcal{L}_4 &= G_4(\phi, X)R + G_{4,X}\left[(\Box\phi)^2 - (\nabla_\mu\nabla_\nu\phi)(\nabla^\mu\nabla^\nu\phi)\right] && (5.15)\\
\mathcal{L}_5 &= G_5(\phi, X)G_{\mu\nu}(\nabla^\mu\nabla^\nu\phi) - && (5.16)\\
&- \frac{1}{6}G_{5,X}\left[(\Box\phi)^3 - 3(\Box\phi)(\nabla_\mu\nabla_\nu\phi)(\nabla^\mu\nabla^\nu\phi)\right] -\\
&- \frac{1}{3}G_{5,X}\left[(\nabla^\mu\nabla_\alpha\phi)(\nabla^\alpha\nabla_\beta\phi)(\nabla^\beta\nabla_\mu\phi)\right]
\end{aligned}$$

where $K(\phi, X)$ is a non-canonical kinetic term, which is a function of ϕ and of the kinetic energy $X = -\partial^\mu\phi\partial_\mu\phi/2$, $G_i(\phi, X)$ (i = 3, 4, 5) are arbitrary coupling functions and $G_{i,X}$ are the partial derivatives of G respect to X. We note that the Lagrangian (5.12) covers all the gravitational theories listed below.

- *Quintessence:*
  The Lagrangian for the Quintessence model (2.47) corresponds to the choice:

$$K(\phi, X) = X/2 - V(\phi) \quad , \quad G_3 = 0, \tag{5.17}$$

$$G_4 = \frac{M_{pl}^2}{2} \quad , \quad G_5 = 0 \tag{5.18}$$

  If we replace the canonical kinetic term X with a non-canonical kinetic term $K(\phi, X)$, we obtain the *K-Essence* model.

- *Brans-Dicke theory:*
  The Lagrangian for Brans-Dicke theory is given by:

$$K(\phi, X) = -\frac{M_{pl}^2\omega_{BD}X}{2\phi} - V(\phi) \quad , \quad G_3 = 0, \tag{5.19}$$

$$G_4 = \frac{M_{pl}^2}{2}\phi \quad , \quad G_5 = 0 \tag{5.20}$$

When $\omega_{BD} = -1$, we have the dilaton gravity model [64].

- *f(R) gravity:* This theory corresponds to the choice:

$$K(\phi, X) = -\frac{M_{pl}^2}{2}(RF - f(R)) \quad , \quad G_3 = 0, \tag{5.21}$$

$$G_4 = \frac{M_{pl}^2}{2}F \quad , \quad G_5 = 0 \tag{5.22}$$

where $F \equiv \partial f / \partial R$.

- *Covariant Galileon theory:*
The Covarian Galileon theory corresponds to the choice:

$$K(\phi, X) = c_2 X \quad , \quad G_3 = c_3 X, \tag{5.23}$$

$$G_4 = \frac{M_{pl}^2}{2} + c_4 X^2 \quad , \quad G_5 = c_5 X^2. \tag{5.24}$$

where $c_{2,3,4,5}$ are constant.

5.1.1. Linear perturbation equations

Now, we are interested in the evolution of linear perturbations in the *quasi-static limit*. It means that we are considering scales inside the cosmological horizon, so we have that $k/(aH) \gg 1$, and also inside the Jeans length of the scalar field, i.e. $c_s k \gg 1$. In this way, we neglect the time-derivative of the scalar field respect to the space-derivative.
As shown in several papers (e.g. [65, 66, 67]), a generic modification of gravity introduces at linear perturbation level two new functions that depend only on background time-dependent quantities and, in Fourier space, on the wavenumber k. One function, that we denote with $Y(t, k)$, represents the ratio between the effective gravitational constant G_{eff} and the Newton constant G for matter and it modifies the standard Poisson equation:

$$Y(a, k) \equiv -\frac{2k^2\Psi}{3(aH)^2\Omega_m\delta_m} \tag{5.25}$$

where Ψ is the gravitational potential which perturbs the temporal part of the FRW metric.
The second one, $\eta(t, k)$, the anisotropic stress or tilt, provides the relation between the two gravity potentials Ψ, Φ:

$$\eta \equiv -\frac{\Phi}{\Psi} \tag{5.26}$$

In standard gravity, one has $Y = \eta = 1$.
For the Horndeski theory, the two functions η and Y take a particularly simple form [66]:

$$\eta = h_2 \left(\frac{1 + k^2 h_4}{1 + k^2 h_5} \right) \tag{5.27}$$

$$Y = h_1 \left(\frac{1 + k^2 h_5}{1 + k^2 h_3} \right) \tag{5.28}$$

where $h_i (i = 1...5)$ are generic functions of ϕ and X respect to the time, all evaluated on the background.
For ΛCDM model, one has simply $h_{1,2} = 1$ and $h_{3,4,5} = 0$.
For the *K-Essence* model (which corresponds to the choices (5.18)), we have that $\eta = 1$ and $Y = 1$, so there aren't modified-gravity effects.
For the evolution of density perturbations, assuming always the quasi-static limit, we have:

$$\delta_m'' + (2 + \frac{E'}{E})\delta_m' = \frac{3}{2}\Omega_m \delta_m Y(a, k) \tag{5.29}$$

where $\Omega_m = \Omega_{m0} a^{-3}/E^2$ and $E \equiv H/H_0$. The prime denotes the derivative respect to $N \equiv \ln(\mathrm{a})$ and, for the Horndeski theory, Y is given by (5.28).
In the next Chapter, we will discuss the constraints that we can obtain on modified gravity parameters by using observations of redshift space distortions.

Chapter 6

Observational constraints on modified gravity

Testing possible modifications of gravity at very large scales is currently one of the most interesting research activity in cosmology.
What we want to do is to measure modified gravity parameters, defined in (5.25)-(5.26), with realistic surveys, and to what precision.
As discussed in [68], is possible to use the motion of the light and of non-relativistic test-particle like galaxies to map out the metric functions Ψ and Φ in principle, and therefore η is an observable quantity. However, in order to characterize the configuration of dark energy in our universe, we also have to map the effective Newton's constant Y, which describes the relative size of the energy-density perturbations of dark-energy and dark-matter.

6.1. A model independent approach

One problem that we have when we estimates a parameter is that often one makes explicitly or implicitly several assumptions that might not be warranted by current data [69].
For instance, one often assumes that the behavior of the cosmological model before dark energy domination, i.e. essentially at any time except very recently, is the standard radiation and matter dominated universe. While we have at least some proof that the radiation epoch had to be close to standard, otherwise one would see deviations from the standard big bang nucleosynthesis and on the microwave background sky, we have much less robust data concerning the matter dominated era, in particular between decoupling and now. For instance, models in which the dark energy was a substantial fraction of the cosmic energy at high redshift [70, 71] cannot yet be excluded.
We identify in particular three assumptions that are very commonly made (at

least one of them is included in, for instance, [72, 73, 74, 75, 76, 77, 78, 79]) and which are certainly acceptable in some cases but that, in reality, are not necessarily warranted in more general gravity theories.
First, we do not know what is the present value of the matter density fraction $\Omega_{m,0}$. If we take it from distance measurements (supernovae, baryon acoustic oscillation) then one should be aware that the observed quantity is the expansion rate $H(z)$ and not the equation of state $w(z)$ or $\Omega_{m,0}$. In fact, the EOS $w(z)$ depends on assuming a value of $\Omega_{m,0}$, and viceversa [80]. Of course if $w(z)$ is parametrized by a small number of parameters then one can get also $\Omega_{m,0}$ from the distance data, but the estimation will depend on the chosen parametrization. Moreover, $\Omega_{m,0}$ cannot be determined without ambiguity with other techniques, e.g. from weak lensing (e.g. [81]) or X-ray temperature in clusters (e.g. [82]), since these estimates always assume standard Newtonian gravity.
Second, we do not know what is the present value of the power spectrum amplitude σ_8. In fact, any estimate of σ_8, through e.g. weak lensing (see e.g. [81]), cosmic microwave background (e.g. [83]), or cluster abundances (see e.g. [82], [1]), depends again on assuming a particular (normally, Newtonian), theory of gravity.
Third, when we obtain the theoretical behavior of linear perturbations, by integrating the matter conservation equations (5.29), we need to assume some initial condition for the matter density contrast δ_m and the peculiar velocity divergence θ_m (or equivalently on δ_m and δ'_m). Typically, this problem is bypassed assuming that the evolution in the past (say, for redshifts $z \gg 1$) was identical to a matter dominated universe so that $\delta_m \sim a$ and $\delta'_{in} = \delta_{in}$ (of course since we are in the linear regime one can always choose freely one of the two initial conditions, say δ_{in}). However, if we do not know the cosmological model in the past, we cannot fix δ'_{in}.
For instance, in some coupled dark matter-dark energy model the perturbations grow faster than in ΛCDM during the matter epoch due to the fact that the dark energy field is not negligible (e.g. [84]); in this case $\delta'_{in} > \delta_{in}$. Similarly, in a Brans-Dicke model with coupling ω one has $\delta'_{in} = (2+\omega)\delta_{in}/(1+\omega)$ [85]; although ω has to be very large to pass local gravity constraints, if a screening mechanism is present these bounds becomes very weak. An initial condition different from the standard case $f = 1$ occurs also in some bigravity model (see e.g. [86]).
Now we want to examine what constraints one can still get on modified gravity, in particular on Y, when all three assumptions, on $\Omega_{m,0}, \sigma_8$ and δ'_{in}, are lifted by marginalizing over all the non-degenerate parameters.
We will consider both current data and forecasted data from a future ex-

periment that approximates the Euclid[1] survey [87]. We call this a *model-independent approach*, although of course we are still making several model-dependent assumptions, like for instance that we are really dealing with linear scales in the sub-horizon regime and that matter is conserved.
We also assume for simplicity that matter is a pressureless fluid and that the background is well approximated by a ΛCDM behavior during the redshift range that we consider. These assumptions can be generalized by adding more parameters, for instance the dark energy equation of state at the present time w_0, its time derivative, and its sound speed, and we expect of course that the results will also depend on the new parameters. One has also to bear in mind that it is possible to modify gravity leaving the function Y unaltered (but not η, when properly defined in the Jordan frame, see discussion in [88]) so that even finding $Y = 1$ does not guarantee Einsteinian gravity.

6.2. Redshift Space Distortion observations

Galaxy surveys measure the redshift of galaxies, in order to provide the redshift space galaxy distributions. From those measurements, is possible to extract the position of the galaxies. However, the inferred galaxy distribution (and the power spectrum) is distorted with respect to the galaxy distributions in real space, since in redshift space one takes into account the peculiar velocities of the galaxies. These are the so called *redshift space distortions*.
From linear perturbation theory and introducing a linear galaxy bias b, the relation between the power spectrum in redshift space P_{red} and the power spectrum in real space reads:

$$P_{red}(\mathbf{k}) = \left(1 + \beta\mu_k^2\right)^2 P(\mathbf{k}) \tag{6.1}$$

where $\beta \equiv f/b$, f is the growth-rate defined as $f = d\log\delta_m/d\log a$ and μ_m is the cosine of the angle between the line of sight and the wavevector $\mathbf{k}$.
When $\mathbf{k}$ is perpendicular to the line of sight, the perturbations are not distorted. The relation given by Eq. (6.1) was first derived by Kaiser [89] and it can be obtained from the continuity equation, which relates the divergence of the peculiar velocity to the dark matter overdensity δ_m. Redshift space distortions, then, relate peculiar velocities to the logarithmic derivative of the linear growth factor, f [90]. A measurement of $\beta \equiv f/b$ will provide information on the growth of structure formation if the galaxy bias b is known.
In our analysis we build a data posterior by using two datasets, the *current*

[1] http://www.euclid-ec.org

dataset and the *forecast dataset*. The current dataset includes all the independent published estimates of $f\sigma_8(z)$ obtained with the redshift distortion method. It includes the data from 2dFGS, 6dFGS, LRG, BOSS, CMASS, WiggleZ and VIPERS, and spans the redshift interval from $z = 0.07$ to $z = 0.8$, see Table 6.1 (see also [76, 81]). In some case the correlation coefficient between two samples has been estimated in Ref. [76] and included in our analysis; when there are different published results from the same dataset in Table 6.1 we include only the more recent one.
The forecast dataset approximates instead the accuracy of a future Euclid mission [87, 91] and it has been obtained in Ref. [68] in the range from $z = 0.5$ to $z = 2.1$.

6.3. Likelihood Analysis

First of all, we rewrite Eq. (5.29) in this way:

$$\delta_m'' + (2 + \frac{E'}{E})\delta_m' = \frac{3}{2}\frac{\delta_m}{a^3E^2}\Omega_{m,0}Y(a,k) \tag{6.2}$$

where we have substitute the expression for Ω_m. This shows immediately that $\Omega_{m,0}$ is fully degenerate with Y. In the following therefore we will only be able to constrain the quantity

$$\hat{Y} \equiv \Omega_{m,0}Y \tag{6.3}$$

Since our reference model is ΛCDM with $\Omega_{m,0}^{(bg)} = 0.3$, the standard value of $\hat{Y}$ is 0.3.
We also rewrite Y for Horndeski theory (5.28) in this way:

$$Y = h_1\frac{1 + (k/k_p)^2h_5}{1 + (k/k_p)^2h_3} \tag{6.4}$$

where the scale k_p is an arbitrary pivot scale that we choose to be $k_p = 1h/\text{Mpc}$. Similarly, when we take this specific Horndeski form (6.4), we will constrain the combination $\hat{h}_1 \equiv \Omega_{m,0}h_1$.
Now, the rate E itself can be estimated with distance indicators only up to some uncertainty. In the following however we will simplify our task by assuming that the error on E is actually already now negligible with respect to the errors on the other observational data. For current data this is not completely true so our estimate of the uncertainty on Y is actually a lower limit. As the main effect of a change in E is through the left-hand-side factor E^{-2} in Eq. (6.2), one can estimate the additional error on $\hat{Y}$ induced

by an error ΔE in E to be $|\Delta\hat{Y}|/\hat{Y} \approx 2|\Delta E|/E$, to be added in quadrature. Current supernovae can determine E around $z \approx 1$ with a relative error of 5-10%, so we can estimate an additional error on $\hat{Y}$ around 10-20%. Since the uncertainty we find is quite larger than this, we neglect the additional source of error from E. For the future data, one can indeed assume that E will be pretty fairly well determined up to better than a percent accuracy with future surveys and our lower limit will be closer to reality.
For the initial conditions on δ_m, we fix the irrelevant value $\delta_{in} = e^{N_{in}}$ with $N_{in} = -1.5$ i.e. $z_{in} \approx 3.5$, while for the initial growth rate parameter $\alpha = \delta'_{in}/\delta_{in}$ we either fix it to unity (standard ΛCDM) or adopt a uniform prior large enough to cover all the region in which the likelihood is significantly different from zero.

6.3.1. Marginalization over σ_8

The growth rate data are given as a set of values d_i at various redshifts, where

$$d_i = f(z_i)\sigma_8(z_i) = f(z_i)\sigma_8 G(z_i) = \sigma_8 \frac{\delta'}{\delta_0} \tag{6.5}$$

and where $f(z) = \delta'_m/\delta_m$ is the growth rate, $G(z)$ is the growth factor normalized to unity today and σ_8 is the present power spectrum normalization. We denote our theoretical estimates as $t_i = \delta'_i/\delta_0$.
Then we build the χ^2 function

$$\bar{\chi}^2_{f\sigma_8} = (d_i - \sigma_8 t_i) C^{-1}_{ij} (d_j - \sigma_8 t_j) \tag{6.6}$$

where C_{ij} is the covariant matrix of the data.
The first step to implement our model-independent estimates is to marginalize over σ_8, since as already mentioned to estimate its value from current data one would need to know the gravitational theory. Marginalizing the likelihood $L' = \exp(-\bar{\chi}^2_{f\sigma_8}/2)$ over $\sigma_8 > 0$ with uniform prior leads to a new posterior $L = \exp(-\chi^2_{f\sigma_8}/2)$ [3] where

$$\chi^2_{f\sigma_8} = S_{dd} - \frac{S^2_{dt}}{S_{tt}} + \log S_{tt} - 2\log(1 + \mathrm{Erf}(\frac{S_{dt}}{\sqrt{2S_{tt}}})) \tag{6.7}$$

and where

$$S_{dt} = d_i C^{-1}_{ij} t_j \tag{6.8}$$
$$S_{dd} = d_i C^{-1}_{ij} d_j \tag{6.9}$$
$$S_{tt} = t_i C^{-1}_{ij} t_j \tag{6.10}$$

This is the posterior distribution we will use in the following discussion.

Survey	z	$f(z)\sigma_8(z)$	References
6dFGRS	0.067	0.423 ± 0.055	Beutler et al. (2012) [92]
LRG-200	0.25	0.3512 ± 0.0583	Samushia et al (2012) [93]
	0.37	0.4602 ± 0.0378	
LRG-60	0.25*	0.3665±0.0601	Samushia et al (2012) [93]
	0.37*	0.4031±0.0586	
BOSS	1) 0.30	0.408± 0.0552, $\rho_{12} = -0.19$	Tojeiro et al. (2012)[94]
	2) 0.60	0.433± 0.0662	
WiggleZ	1) 0.44	0.413 ± 0.080, $\rho_{12} = 0.51$	Blake (2011) [95]
	2) 0.60	0.390 ± 0.063, $\rho_{23} = 0.56$	
	3) 0.73	0.437 ± 0.072	
Vipers	0.8	0.47 ± 0.08	De la Torre et al (2013)[96]
2dFGRS	0.13	0.46 ± 0.06	Percival et al. (2004) [97]
LRG	0.35	0.445 ± 0.097	Chuang and Wang (2013) [98]
LOWZ	0.32	0.384±0.095	Chuang at al (2013) [99]
CMASS	0.57*	0.348 ± 0.071	
	0.57*	0.423 ± 0.052	Beutler et al (2014)[100]
	0.57	0.441±0.043	Samushia et al (2014) [77]
	0.57*	0.450 ± 0.011	Reid et al (2013) [101]

Table 6.1: Current published values of $f\sigma_8(z)$. In some cases we list also the correlation coefficient ρ_{ij} between different bins [76]. Entries with an asterisk are not employed in this analysis.

6.4. Current growth-rate data

Current growth data are not sufficient to provide k-dependent information. In this case, therefore, we are forced to neglect the k-dependence of Y.
Moreover, again in view of the lack of sufficient statistics, we also fix the time dependence and assume that Y is just a constant over the redshift range of the observations. We have therefore just two parameters: $\hat{Y}$ and the initial condition α.
We will consider four cases, in increasing order of "model independence".
The *first case* is standard ΛCDM gravity ($Y = 1$), and σ_8 and initial conditions both fixed to the fiducial model, $\sigma_8 = 0.83$ [83] and $\alpha = 1$. Here the only free parameter is therefore $\Omega_{m,0}$ (with an uniform prior in $0, 1$).
The *second case* is like the first one but with marginalization over σ_8. This case serves mainly to isolate the effect of the σ_8-marginalization and to see how much the best fit of $\Omega_{m,0}$ changes if σ_8 is estimated from the $f\sigma_8(z)$ data themselves and not from Planck. From now on, we always fix the background evolution E to a ΛCDM with $\Omega_{m,0}^{(bg)} = 0.3$, in agreement with observations and close to the Planck best fit [83], and neglecting any uncertainty on it and we always include the marginalization over σ_8.
In the *third case*, beside marginalizing over σ_8, we leave $\hat{Y}$ free to vary with an uniform prior for positive values.
Finally, the *fourth case* is like the third one but now the initial growth rate α is left free to vary.

6.4.1. Results

The results for the first and second cases are shown on the left panel of Fig. (6.1). At 68% c.l., the uncertainty on $\Omega_{m,0}$ increases from 0.03 to roughly 0.10 when marginalizing over σ_8 while for σ_8 itself we find $\sigma_8 = 0.76^{+0.06}_{-0.10}$, smaller than but compatible with the Planck value. On the right panel, we plot the $f\sigma_8$ data points from the galaxy surveys with their respective error bars in comparison with the ΛCDM model and with the best fits of all the cases.
In the third case (uniform prior on $\hat{Y}$, fixing $\alpha = 1$) we find a best fit $\hat{Y} = 0.20$ with an error range $[0.095, 0.36]$ at 68% confidence level, see Fig. (6.2) bottom left panel. The parameter σ_8 is now $\sigma_8 = 0.79^{+0.11}_{-0.25}$, see Fig. (6.3). If

now we vary α with a uniform prior on $\hat{Y}$ (fourth case, Fig. 6.2) we obtain instead $\hat{Y} = 0.28$ with a doubled error range $[0.048, 0.63]$ at 68% c.l. . For σ_8 we have now $\sigma_8 = 0.54^{+0.21}_{-0.09}$. Table (6.2) summarizes the results.
Interestingly, we detect a bimodality in the marginalized posterior for α and a strong correlation with $\hat{Y}$. As shown in Fig. (6.2) both very large and very small values of $\hat{Y}$ are acceptable if α varies freely. In particular, a large $\hat{Y}$ can be compensated by a large negative α, while small $\hat{Y}$ are compatible with large positive values. Large negative values of α mean that overdensities can become underdensities at some point in time; although this might appear pathological at first sight, it does not contradict any observation at linear scales and should not be arbitrarily excluded. Within 3σ, a small $\hat{Y}$ is compatible with any value of α since in this limit the perturbation equation becomes effectively first order in δ'.
The data in Table 6.1 have been obtained with cosmologies close to our reference one, but not identical. We repeated the analysis of these four cases by first converting the $f\sigma_8(z)$ data to the same cosmological background data (obtained by putting $\Omega_{m,0}$ and $\hat{Y}$ to the best fit in the definition of d_i, see Eq. (6.5)) in order to see how this issue affects the outcome of the statistical analysis. This method has been employed in the past in [102] for $\sigma_8(z)$ and in [103] for $f\sigma_8(z)$. We found that the relative errors on $\Omega_{m,0}$, $\hat{Y}$ and σ_8 change only by 10% at most with respect to the previous results (Table 6.2).
The conclusion of this section is that current data put hardly any constraint on $\hat{Y}$. Any value from 0 to 1.35 is acceptable at 95% and much larger values of $\hat{Y}$ are also acceptable if the initial condition is chosen along the degeneracy line of Fig. (6.2). This conclusion could have been reasonably expected due to the paucity of present data.
In the next section we show however that the constraints improve a lot with the much better data of future surveys only if we keep α fixed; in the more general case, the improvement remains modest. The reason is the same: trying to be as much model-independent as possible one has to set $\sigma_8, \Omega_{m,0}, \alpha$ free to vary. The price to pay for this freedom are rather weak constraints.

6.5. Forecast data

A. z binning

In this section we consider the forecast Euclid-like $f\sigma_8$ datasets, starting with the case of no scale information (z-binning), which can be directly compared to the previous ones. The growth forecasts are obtained from Ref. [68].
We consider a Euclid-like 15,000 square degrees redshift survey from $z =$

	case	α (best fit)	$\Delta\alpha$ (95%)	$\Delta\alpha$ (68%)
ΛCDM, $Y = 1$, σ_8 =0.83	I	1	-	-
ΛCDM, $Y = 1$, marg. on σ_8	II	1	-	-
Unif. prior on $\hat{Y}$	III	1	-	-
Unif. prior on $\hat{Y}, \alpha$	IV	-0.015	$\leq$-2.08 and $\geq$ -0.67	[-0.40, 1.32] and [-4.05, -2.20]

	case	$\Omega_{m,0}^{(bg)}$ (best fit)	$\Delta\Omega_{m,0}^{(bg)}$ (95%)	$\Delta\Omega_{m,0}^{(bg)}$ (68%)
ΛCDM, $Y = 1$, σ_8 =0.83	I	0.23	[0.18, 0.29]	[0.20, 0.26]
ΛCDM, $Y = 1$, marg. on σ_8	II	0.27	[0.12, 0.54]	[0.18, 0.39]
Unif. prior on $\hat{Y}$	III	-	-	-
Unif. prior on $\hat{Y}, \alpha$	IV	-	-	-

	case	$\hat{Y}$ (best fit)	$\Delta\hat{Y}$ (95%)	$\Delta\hat{Y}$ (68%)
ΛCDM, $Y = 1$, σ_8 =0.83	I	-	-	-
ΛCDM, $Y = 1$, marg. on σ_8	II	-	-	-
Unif. prior on $\hat{Y}$	III	0.20	[0.040, 0.60]	[0.095, 0.36]
Unif. prior on $\hat{Y}, \alpha$	IV	0.28	[0, 1.35]	[0.048, 0.63]

TABLE 6.2: Summary of results for current data.

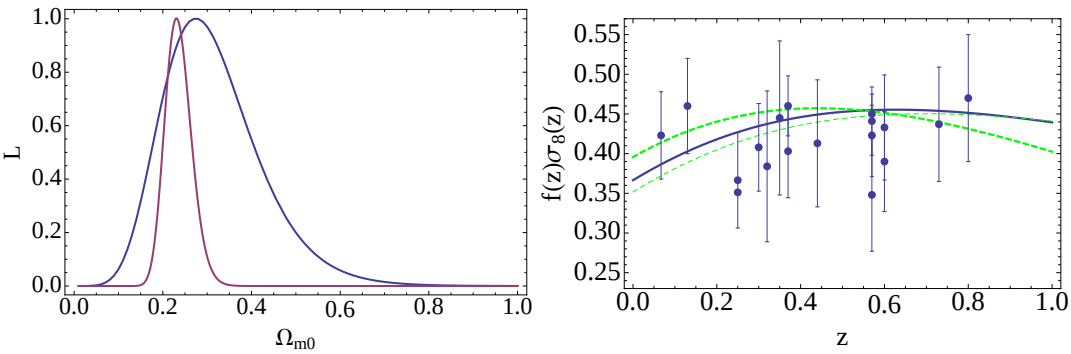

FIGURE 6.1: *Left panel* : Current posterior in function of $\Omega_{m,0}$ for the first case (red curve) and for the second case (blue curve). *Right panel* : Best fit ΛCDM model for the first case (blue solid curve); best fit for the third case (green thin dashed curve) and for the fourth case (green thick dashed curve) together with the entire set of $f\sigma_8$ data points we employed in this paper. As the posterior is marginalized over σ_8, a possible vertical rescaling for the third and fourth cases is inconsequential so they have been plotted with a normalization that minimizes the χ^2 distance.

$0.5 - 1.5$ divided in equally spaced bins of width $\Delta z = 0.2$ and, in order to prevent accidental degeneracy due to low statistic, a single larger redshift bin between $z = 1.5 - 2.1$, so in total we have six bins. In Table 6.3 we show the fiducial values and relative errors on $f\sigma_8$. As before, we want to obtain an

$\bar{z}$	$f\sigma_8$	$\Delta f\sigma_8$ (68% c.l.)
0.6	0.469	0.0092
0.8	0.457	0.0068
1.0	0.438	0.0056
1.2	0.417	0.0049
1.4	0.396	0.0047
1.8	0.354	0.0039

TABLE 6.3: Fiducial values and Euclid-like errors for $f\sigma_8$ using six redshift bins (from [68]).

estimate on a constant $\hat{Y}$ marginalizing over σ_8 and α. Fig. (6.4), lower left panel, shows the 1-dimensional marginalized *forecast posterior* distribution of Y (third case) along with the fourth case, i.e. with marginalization over α. As can be seen from Fig. (6.4), lower left panel, the 95% error on $\hat{Y}$ around

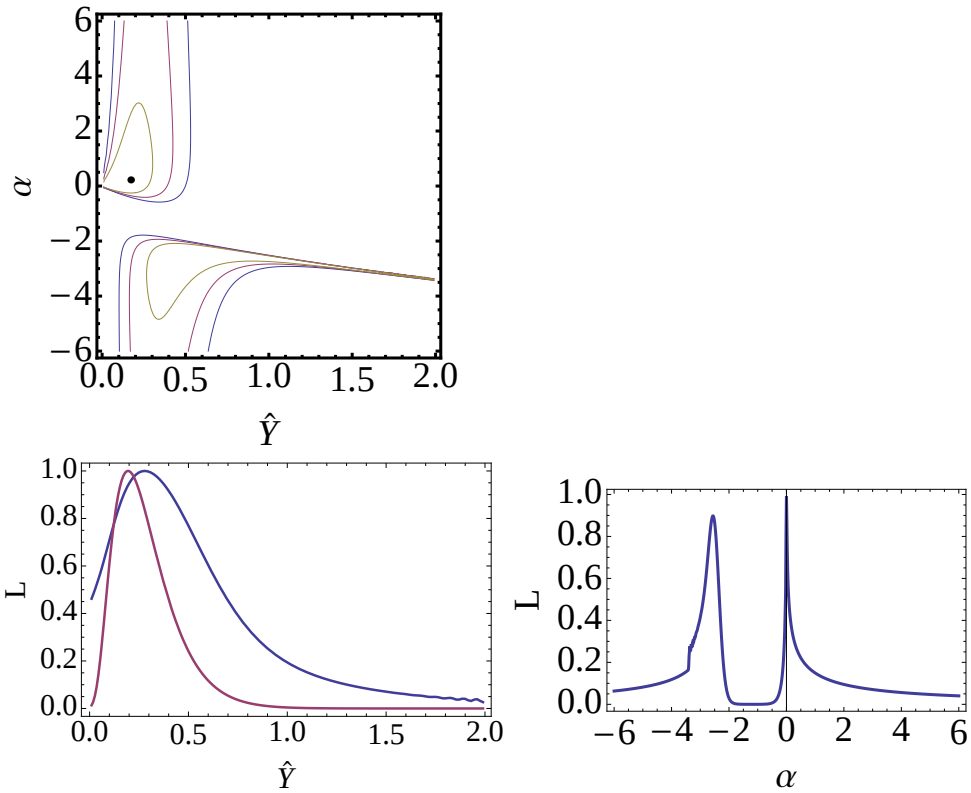

FIGURE 6.2: *Top panel*: 1σ, 2σ and 3σ confidence-level contours for the 2-dimensional current posterior on the parameters $\{\hat{Y},\alpha\}$ marginalizing over σ_8 (fourth case). *Left bottom panel* : Current posterior for $\hat{Y}$ marginalized over α (blue line) in comparison with the third case (red line). *Right bottom panel* : Current posterior for α marginalized over $\hat{Y}$.

the fiducial value 0.3 has a fivefold increase, from 0.03 to roughly 0.15, when we marginalize over the initial conditions. The relative uncertainly on $\hat{Y}$ is around 30% at 68% c.l..

Contrary to what we found previously using current data, negative values of α appear now strongly disfavoured. The increase in errors on both $\hat{Y}$ and σ_8 can be appreciated from Fig. (6.5). In the third case (i.e. no marginalization over α) future Euclid-like data can estimate σ_8 and $\hat{Y}$ to within 0.01 for both parameters; when α is marginalized over however the error increases to roughly 0.08, again for both parameters.

	case	α (best fit)	$\Delta\alpha$ (95%)	$\Delta\alpha$ (68%)
Unif. prior on $\hat{Y}$	III	1	-	-
Unif. prior on $\hat{Y}, \alpha$	IV	0.53	[0, 4.0]	[0.12, 1.6]

	case	$\hat{Y}$ (best fit)	$\Delta\hat{Y}$ (95%)	$\Delta\hat{Y}$ (68%)
Unif. prior on $\hat{Y}$	III	0.29	[0.26, 0.32]	[0.28, 0.30]
Unif. prior on $\hat{Y}, \alpha$	IV	0.30	[0.12, 0.43]	[0.21, 0.38]

Table 6.4: Summary of results for forecasted Euclid data.

$\bar{z}$	$k_{min} - k_1$	$k_1 - k_2$	$k_2 - k_{max}$
0.6	0.007-0.022	0.022-0.063	0.063-0.180
0.8	0.007-0.023	0.023-0.071	0.071-0.215
1.0	0.007-0.024	0.024-0.078	0.078-0.249
1.2	0.007-0.026	0.026-0.086	0.086-0.287
1.4	0.007-0.027	0.027-0.094	0.094-0.329
1.8	0.007-0.029	0.029-0.112	0.112-0.426

Table 6.5: Ranges of the k-bins for every redshift bin centered at $\bar{z}$, in units of (h/Mpc) (from [68]).

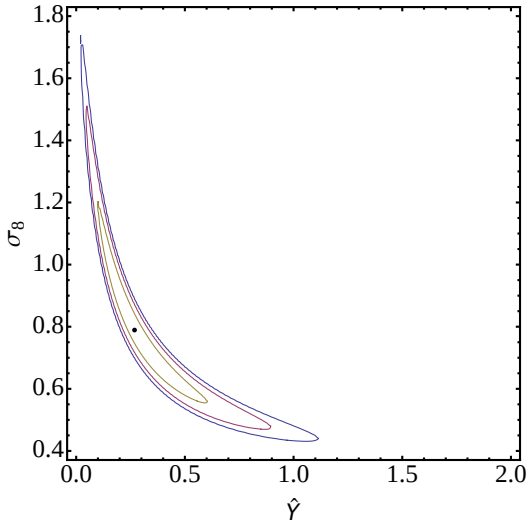

FIGURE 6.3: 1σ, 2σ and 3σ confidence-level contours for the current posterior on the parameters $\{\hat{Y},\sigma_8\}$ (third case).

B. k BINNING

We consider now the quasi-static Horndeski result, defined in Eq. (6.4), which contains the parameters h_1, h_3 and h_5 and a $k-$dependence. Although in general these parameters depend on time, we assume here for simplicity that they time variation is negligible in the observed range.
The aim of this section is to obtain error estimates on the Horndeski parameters, so we need to have a minimum of three k-bins for every value of the redshift. The fact that a Euclid-like mission is capable of delivering data with non-vanishing constraining power in several k-bins is indeed an important advantage of this kind of large scale project and a crucial feature if one wants to test modified gravity with sufficient generality. It is in fact the only way to detect a possible k-dependence as predicted within the Horndeski class. In other words, if all the k bins are lumped together, as in the standard way of presenting current observational data, then it is impossible to detect the k-structure of $Y(z,k)$.
Again following the method of [68], we take the minimum binning value of k as $k_{min} = 0.007\ h/Mpc$ (the result is very weakly dependent on this value) and the values of the highest k are chosen to be well below the scale of non-linearity at the redshift of the bin. In Table 6.5 we report the k-bin boundaries. In Table 6.6 we display the fiducial values and errors for $f\sigma_8$ at every redshift and every k- bin. As in the previous case, also here the fiducial model is chosen to be ΛCDM, so the fiducial values for the Horndeski

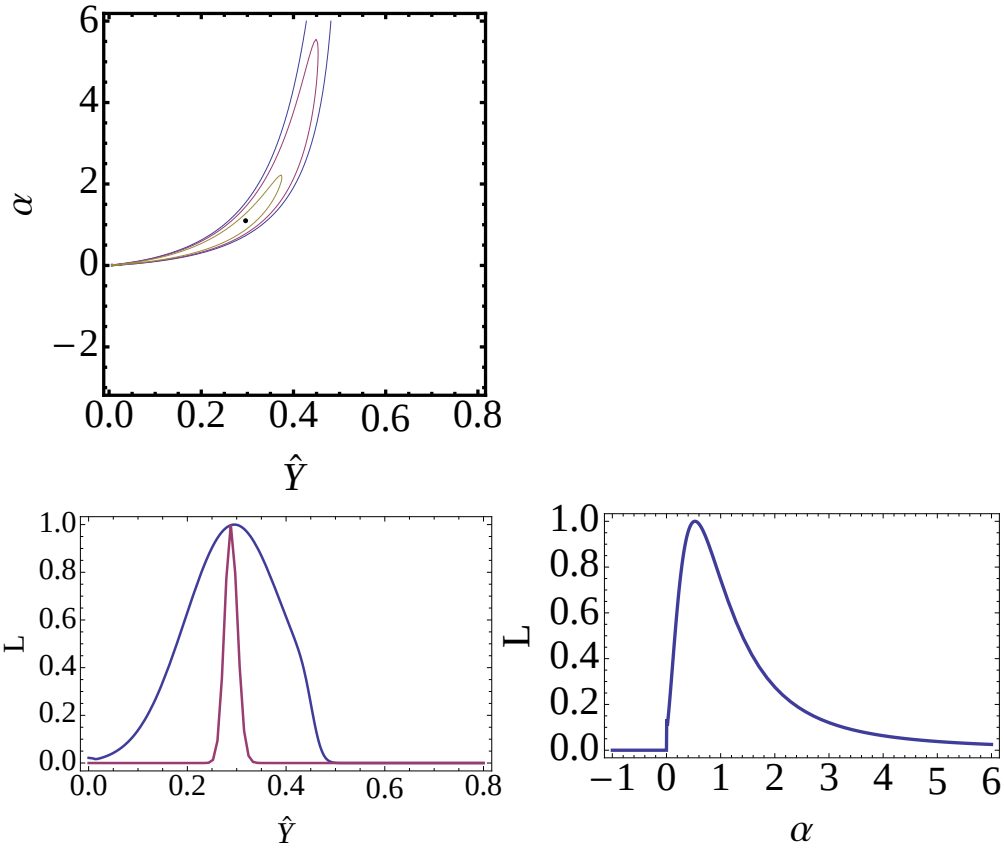

Figure 6.4: *Top panel* : 1σ, 2σ and 3σ confidence-level contours for the 2-dimensional forecast posterior on the parameters $\{\hat{Y},\alpha\}$ marginalizing over σ_8 (fourth case). *Left bottom panel* : forecast posterior for $\hat{Y}$ marginalized over α (blue line) in comparison with the third case (red line). *Right bottom panel* : forecast posterior for α marginalized over $\hat{Y}$

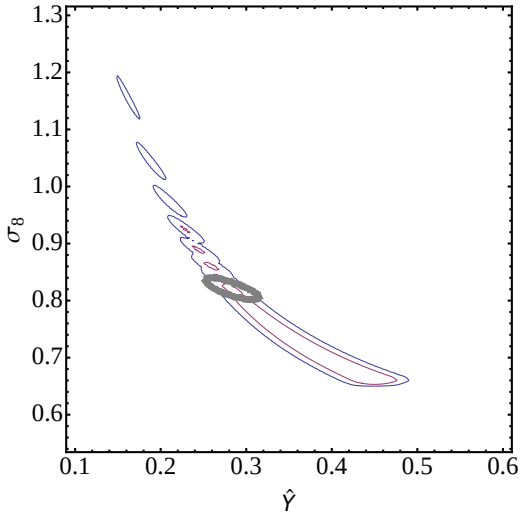

FIGURE 6.5: 1σ and 2σ confidence-level contours for the forecast posterior on the parameters $\{\hat{Y},\sigma_8\}$ when α is marginalized over (fourth case, solid curves) and when is fixed (third case, small gray ellipse, only the 2σ contour is shown).

parameters are $\hat{h}_1 = \Omega_{m,0}h_1 = 0.3$ and $h_3 = h_5 = 0$. Here we fix h_5 to its fiducial value (i.e. to zero) due to the degeneracy between h_5 and h_3 when the fiducial model is such that $h_5 = h_3$ as in ΛCDM. In the next section we will consider the case in which the fiducial value of h_5 is different from the standard value.

The model now contains three parameters: $\{\hat{h}_1, h_3, \alpha\}$. Note that in principle one should take a different α for every k but for simplicity we assume that α is k-independent in our range. As in the previous cases, here we analyze first the case in which $\alpha = 1$ (this is our *fifth case*) and the case in which we will vary this parameter (*sixth case*). We numerically solve Eq. (5.29) inserting now the value of k corresponding to the central k-bin values for every redshift bin and then we construct the σ_8-marginalized three dimensional forecasted posterior by following the same procedure described in section III. The results are reported in Tables 6.7, 6.8, 6.9 and in Figs. (6.6,6.7). The error on $\hat{h}_1$ increase from roughly 0.02 to 0.10 when marginalizing over the initial condition. In contrast, the error on the scale h_3 remain practically unchanged, since we assume k-independent initial conditions.

$\bar{z}$	i	$f\sigma_8(z)$	$\Delta f\sigma_8(z)$	$\Delta f\sigma_8(z)\%$
	1		0.07	15
0.6	2	0.469	0.017	3.6
	3		0.0097	2.1
	1		0.05	11
0.8	2	0.457	0.012	2.6
	3		0.0074	1.6
	1		0.039	8.9
1.0	2	0.438	0.0089	2
	3		0.0062	1.4
	1		0.032	7.7
1.2	2	0.417	0.0072	1.7
	3		0.0055	1.3
	1		0.028	7
1.4	2	0.396	0.065	1.6
	3		0.0057	1.4
	1		0.015	4.3
1.8	2	0.354	0.0047	1.3
	3		0.0061	1.7

Table 6.6: Fiducial values and relative errors for $f\sigma_8$ data at every redshift $\bar{z}$ and every k-bin (labeled with the index i).

	case	α (best fit)	$\Delta\alpha$ (95%)	$\Delta\alpha$ (68%)
Horndeski	V	1	-	-
Horndeski	VI	0.85	[0.10, 2.2]	[0.22, 1.9]

Table 6.7: Best fit and errors on α in the Horndeski case by fixing $h_5 = 0$.

	case	$\hat{h_1}$ (best fit)	$\Delta\hat{h_1}$ (95%)	$\Delta\hat{h_1}$ (68%)
Horndeski	V	0.3	[0.26, 0.32]	[0.27, 0.32]
Horndeski	VI	0.3	[0.097, 0.44]	[0.17, 0.40]

Table 6.8: Best fit and errors on $\hat{h_1}$ in the Horndeski case by fixing $h_5 = 0$.

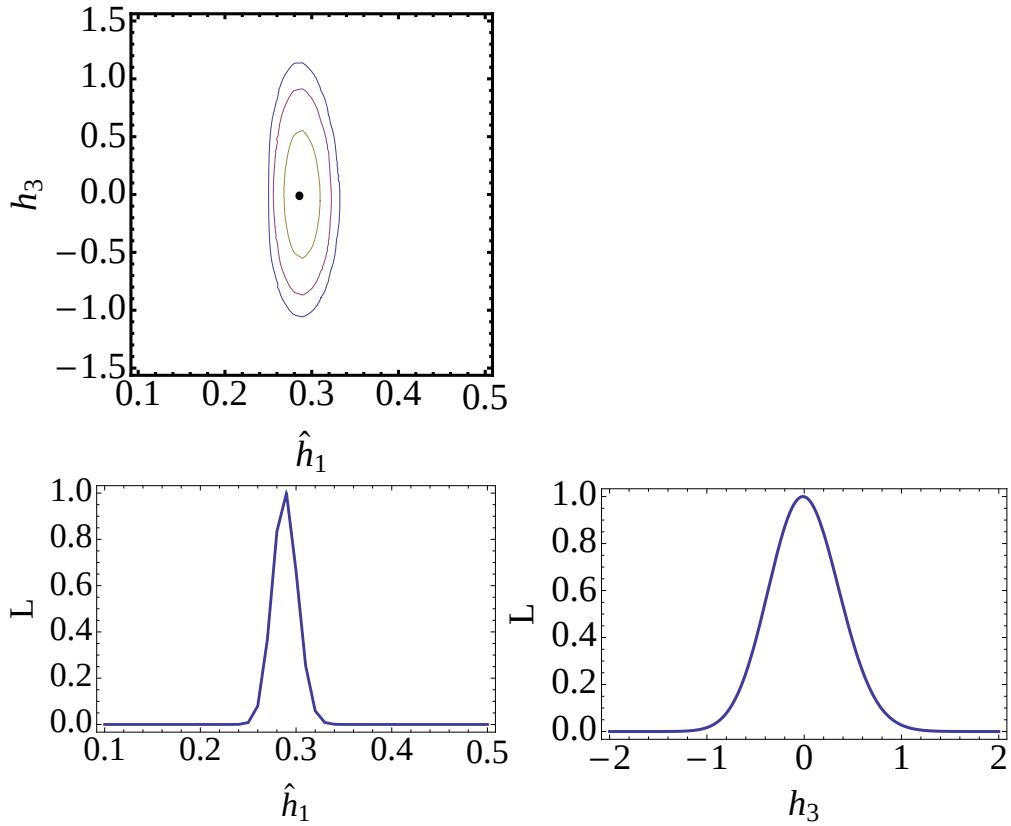

FIGURE 6.6: *Top panel* : 1σ, 2σ and 3σ confidence-level contours for the 2-dimensional forecast posterior on the parameters $\{\hat{h}_1, h_3\}$ marginalizing over σ_8 (fifth case). *Left bottom panel :* forecast posterior for $\hat{h}_1$ marginalized over h_3. *Right bottom panel* : forecast posterior for h_3 marginalized over $\hat{h}_1$.

	case	h_3 (best fit)	Δh_3 (95%)	Δh_3 (68%)
Horndeski	V	0	[-0.70, 0.72]	[-0.37, 0.35]
Horndeski	VI	0	[-0.72, 0.73]	[-0.36, 0.36]

TABLE 6.9: Best fit and errors on h_3 in the Horndeski case by fixing $h_5 = 0$.

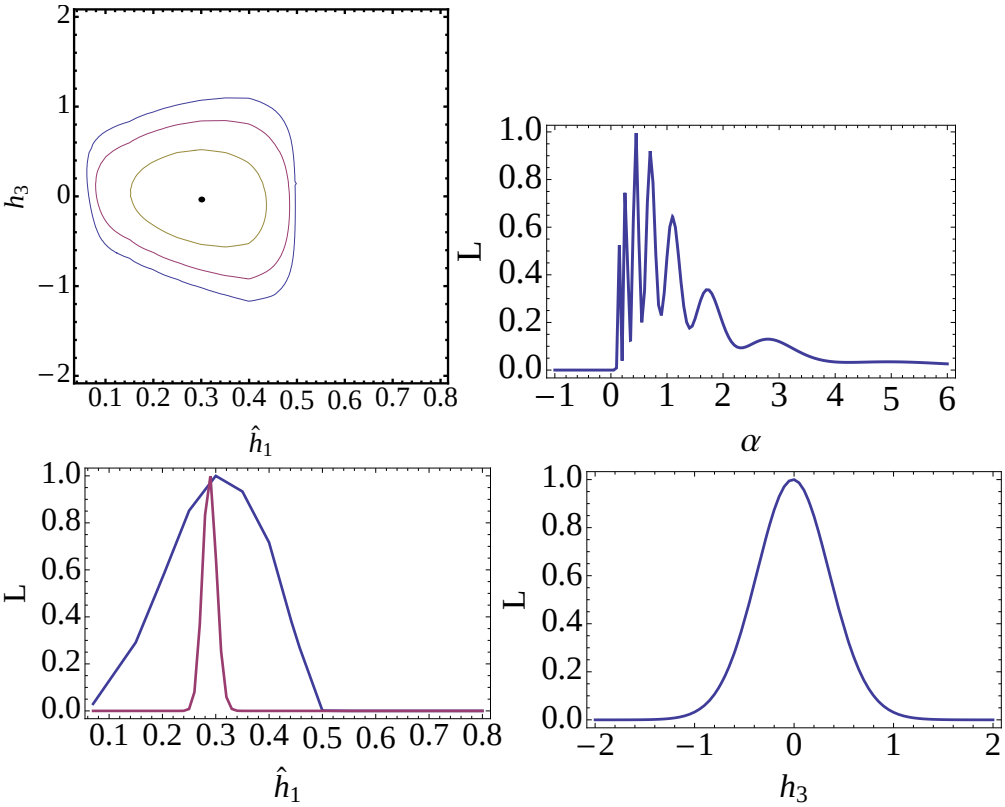

Figure 6.7: *Top panel* : 1σ, 2σ and 3σ confidence-level contours for the 2-dimensional forecast posterior on the parameters $\{\hat{h}_1, h_3\}$ marginalizing on $\{\sigma_8,\ \alpha\}$ (sixth case). *Left bottom panel* : forecast posterior marginalized on $\{h_3, \alpha\}$ varying the initial conditions (blue line) in comparison with the fifth case (red line). *Right bottom panel* : forecast posterior marginalized on $\{\hat{h}_1, \alpha\}$

6.6. A cosmological exclusion plot

Here we wish to continue the analysis by obtaining an exclusion plot, i.e. the region of parameter space that a future Euclid-like redshift survey can achieve. This is obtained by repeating the procedure of the previous section obtaining the errors on $\hat{h}_1, h_3$ for every possible h_5 (rather than fixing h_5 to the standard value). The region outside the errors is therefore the region that an Euclid-like experiment will be able to rule out.
The form of Y in Eq. (6.4) produced in a Horndeski model represents a Yukawa-like gravitational potential in real space. By Fourier anti-transforming Eq. (5.25) with a point source of mass M one obtains in fact

$$\Psi(r) = -\frac{G_0 M}{r} h_1 \left(1 + Q e^{-r/\lambda}\right) \tag{6.11}$$

where $h_5 = (1+Q)\lambda^2$ and $h_3 = \lambda^2$ (notice that here again Mh_1 is the observable, not h_1 alone). Here G_0 is the gravitational constant one would measure in laboratory where, as already mentioned, the effects of the modification of gravity are assumed to be screened [2]. Thus, instead of $h_{3,5}$, we can use the strength Q and range λ of the Yukawa term as modified-gravity parameters, marginalizing over $\hat{h}_1 = \Omega_{m,0} h_1$ and, as before, also over σ_8 and α. As previously, we assume Q, λ to be constant in the observed range.
These parameters are the cosmological analog of the parameters employed in laboratory experiments to test deviations from Newtonian gravity, see e.g. [104]. Using the same specifications of the previous section, we show in Fig. (6.8) the region that a Euclid-like experiment is able to exclude.
Clearly, for very small λ the strength Q is unconstrained; moreover, for very large interaction ranges (much larger than the observed scales), the strength becomes degenerate with h_1 and therefore again weakly constrained.
In the intermediate region around 10 Mpc/h the strength can be confined to within 0.03 (0.06) at 68% (95%) c.l., i.e. 3% (6%) of the Newtonian gravitational strength. This limit is of course much weaker than local gravity bounds, which are below 10^{-4}, but it applies to scales and epochs unreachable with other means. The results will not change much if we do not marginalize over initial conditions, just as it happened for h_3 in the previous section.
For comparison, the strength Q in the case of $f(R)$ models is 1/3 (see e.g.

[2] Notice that although one could define a new gravitational "constant" $G_{\rm eff} = G_0 h_1 (1 + Q e^{-r/\lambda})$ in the potential, one should use a different definition, namely $G^F_{\rm eff} = G_0 h_1 (1 + Q e^{-r/\lambda}(1 + r/\lambda))$, in the force. This is why we prefer to use a different notation, i.e. Y.

[105]), while the range is

$$\lambda_{f(R)} = M_{f(R)}^{-1} = \sqrt{\frac{3 f_{,RR}}{f_{,R}}} \tag{6.12}$$

where the subscripts denote the derivative with respecto to R of the Lagrangian $f(R)$ (in this notation $f(R)$ includes the Einstein-Hilbert term). From Fig. (6.8) one can see that all the models with $2 \lesssim \lambda_{f(R)} \lesssim 80$ Mpc/h could be ruled out at 95% c.l. for $Q = 1/3$.
Conversely, assuming $f_{,R} \approx 1$ as needed by local gravity constraints and by a background close to ΛCDM, a Euclid-like survey will be able to set a lower and an upper limit to $f_{,RR}$:

$$f_{,RR} < 1 \cdot 10^{-7} H_0^{-2}, \quad \text{or} \tag{6.13}$$

$$f_{,RR} > 2 \cdot 10^{-4} H_0^{-2} \tag{6.14}$$

In keeping with our analysis, we are assuming here $\lambda_{f(R)}$ constant; in general however it will be a function of time so these limits should refer to the epoch of observation. In some popular models of $f(R)$ one has $f_{,RR} \approx 10^{-3} H_0^{-2}$ at $z \approx 1$ (see e.g. [106]), corresponding to $\lambda_{f(R)} \approx 100 - 200$ Mpc/h, a value that could be marginally detected at 68% c.l. by our forecasts.
Notice however that in $f(R)$ models the overall factor here denoted as $\hat{h}_1$ corresponds to $\Omega_{m,0}/f_{\prime R} \approx \Omega_{m,0}$. The existence of a lower limit to $f_{,RR}$ is due to the marginalization over the unknown $\Omega_{m,0}$.
In specific models of $f(R)$ the present matter density $\Omega_{m,0}$ can be estimated through background or large-scale structure measurements. In this case the lower limit would be removed and any $\lambda_{f(R)}$ larger than a few Megaparsec would be detected.

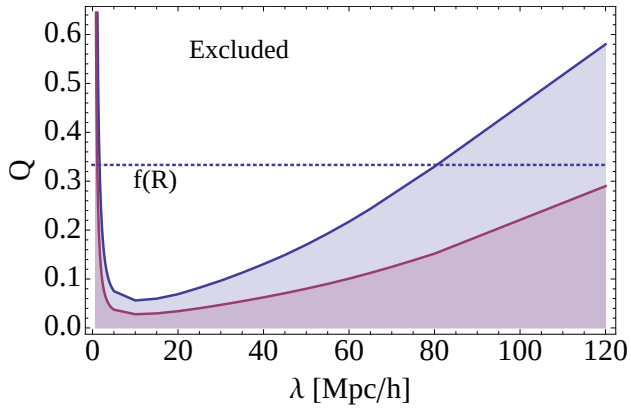

FIGURE 6.8: Forecast of a cosmological exclusion plot for a Euclid-like survey, marginalizing over σ_8, α and $\hat{h_1}$. Here Q is the dimensionless strength of the Yukawa interaction while λ, in Mpc/h, is the interaction range. The darker region is the 68% c.l. region, the lighter one is the 95%. c.l. region. The dotted line marks the value of Q in $f(R)$ models.

Chapter 7

Conclusion

In the first part of this Thesis we have studied the formation of dark matter halos in the symmetron model, where a scalar field metrically coupled to all matter species alters the standard growth of cosmic overdensities. The dynamics of the symmetron is controlled by a Z_2 symmetry (under which this scalar is odd) whose breaking generates a new long-range interaction of gravitational strength.

In Chapter 3, we focused on single spherically symmetric overdensities whose evolution departs from the background expansion before recombination. We followed the time evolution of these objects generalizing the spherical collapse model to include all relevant physical effects related to the new long-range force mediated by the symmetron field.

We identify two distinct scenarios, depending on the initial radius of the collapsing halo. For small initial overdensities, the evolution of the symmetron field inside the forming dark matter halo adiabatically follows during all the phases of the spherical collapse the one of the background scalar field. This implies that in this "thick-shell scenario" the formation of a dark matter halo is affected by the symmetron mediated force from the time of the Z_2 symmetry breaking till the dark matter halo has formed. In this case dark matter halos tend to collapse earlier compared to the ΛCDM case.

In a second scenario, corresponding to large initial overdensities, a transition between the previously described thick-shell regime and the "thin-shell regime" takes place, and the symmetron force is screened in the interior of the collapsing halo before collapse. In this case dark matter halos tend to form later compared to the thick-shell scenario where instead the symmetron force was active till the end of the spherical collapse. Also in this case, however, halos collapse earlier than in the ΛCDM case where the additional long-range scalar force was not present at all.

Then, we have analyzed the statistics of the dark matter halos formed within

the symmetron model, focusing on the calculation of the halo mass function and of the linear bias for the two scenarios identified during the first part of this study. In both cases we have found non-negligible differences comparing the halo mass function and the linear bias obtained within the present realization of the symmetron model to standard ΛCDM results. In the thick-shell scenario, the relative difference between the halo mass function of our model and the one of the ΛCDM can be as large as few percent for halos with a mass between 10^{11} and $10^{13} M_\odot\ h^{-1}$; for virial masses larger than about $10^{13} M_\odot\ h^{-1}$, the halo mass function of the symmetron model tends towards the one of the ΛCDM.
Though the departures from the ΛCDM predictions seem very hard to identify at present, further investigations of the non-linear regime of the overdensity evolution based on dedicated N-body simulations might find additional features which would allow to better disentangle the halo mass function of the symmetron model from the one of the ΛCDM.
In the second part of this thesis, we investigated the current and future bounds on the modified gravity parameter Y (or $G_{\rm eff}$) that quantifies the deviation from the standard Poisson equation. We have assumed Y to be constant in time and space when using current data or with a Horndeski behavior when forecasting future results. Contrary to other similar analyses, we tried to weaken the model-dependency by marginalizing over the present power spectrum normalization σ_8 and over the initial growth rate for the matter density contrast equation, since they both are unknown unless one assumes a specific model, e.g. ΛCDM. We also take into account the fact that $\Omega_{m,0}$ is not a directly observable quantity and absorb it into the definition of Y.
In Chapter 5 we have found, not unexpectedly, that the current growth rate data $f\sigma_8(z)$ from redshift distortion are insufficient to constrain the product $\hat{Y} = \Omega_{m,0} Y$ to better than an order of 100% error (see Table 6.2, fourth case), due to the degeneracy with σ_8 and the initial condition. Using instead forecasts of a Euclid-like experiment, we have found that the relative error on $\Omega_{m,0} Y$ reduce to roughly 30% at 68% c.l. (see Table 6.4, fourth case). A similar error can be obtained on $\hat{h}_1 = \Omega_{m,0} h_1$ when using the Horndeski prescription (see Table 6.8, sixth case). The effect of the lack of knowledge of the initial conditions can be easily grasped by noting that the uncertainty on $\hat{Y}$ increases from $\Delta\hat{Y} \approx 0.01$ when $\alpha = 1$ to $\Delta\hat{Y} \approx 0.08$ when α is marginalized over (Table 6.2), i.e. from a few percent to 30%. Same broadening of the uncertainty occurs for σ_8.
Finally, in the last part of Chapter 5, we have obtained a forecast of a cosmological exclusion plot on the Yukawa strength Q and range λ parameters

(Fig. 6.8). This complements, on cosmological scales, the laboratory exclusion plots on deviations from standard gravity. We have found that with a Euclid-like experiment the strength Q can be confined to within 3%(6%) of the Newtonian gravity at 68%(95%) if the interaction range is around 10 Megaparsecs. For much larger and much smaller ranges the constraint gradually vanishes. Applying these results to $f(R)$ models we forecasted an upper limit to $f_{,RR}$ at $z \approx 1$ of the order of $10^{-7} H_0^{-2}$, corresponding to a Yukawa range smaller than 2 Mpc/h roughly, and a lower limit of $2 \cdot 10^{-4} H_0^{-2}$, corresponding to scales larger than 80Mpc/h (at 95% c.l.).
The main conclusion of this Thesis is that Y can be only weakly constrained by the next decade redshift surveys if one takes into account the degeneracy with $\sigma_8, \Omega_{m,0}$ and initial conditions. Even weaker constraints would have been obtained had we taken Y to be time dependent. Only by considering specific models can one hope to produce stringent constraints on modified gravity through its effect on linear matter perturbation growth. This seems to indicate that the other modified gravity linear perturbation parameter, the anisotropic stress η, which requires a combination of weak lensing and clustering, is a more robust and powerful way to quantify the deviation from standard gravity.

Ringraziamenti

Vorrei prima di tutto ringraziare il mio relatore Massimo Pietroni, per avermi seguita durante questi tre anni e per avermi dato consigli ogni volta che ce n'era bisogno.
Ringrazio poi Luca Amendola, per avermi dato la possibilità di lavorare con lui presso il suo Istituto e insieme al suo fantastico gruppo di "cosmici".
Ringrazio i miei ex colleghi d' ufficio, quelli che mi hanno accolta nel lontano gennaio 2012 e con i quali ho trascorso il mio primo anno di dottorato, ovvero Alessio Camobreco, Luca Franci e Stefano Mori. Ringrazio Alessio per tutte le lunghissime cene fatte a casa sua e Stefano per tutta la sua pazienza e tutta la sua calma dimostrata in questi anni. Un grazie speciale va a Luca Franci, per tutti i momenti passati insieme, per le "pizzate" a casa sua, per le lontane partitine di tennis in cui non ho mai vinto, per le tante risate insieme e per le tante lamentele condivise.
Un grazie di cuore a Michelangelo Preti (Il Micio), per tutte le volte che mi ha fatto scoppiare a ridere durante una triste giornata, per tutte le volte che mi ha aiutata a risolvere problemi con il pc e per non aver mai detto "no". Insieme a lui, ringrazio Enrico Ubaldi (Ubi), anche lui per i suoi preziosi aiuti, per la sua competenza lavorativa e per il suo altruismo e per tutte le cioccolate e i biscottini offerti durante i pomeriggi in ufficio. Non potevo avere colleghi e compagni d'ufficio migliori.
Un grazie speciale va a Chiara, per aver condiviso tanti momenti insieme e per aver legato fin da subito, Pietro, per tutte le iniziative organizzate durante questi anni e per la sua positività, e Max, per la sua disponibilità e il suo altruismo.
Un grazie anche a tutti gli altri dottorandi, compagni di pranzi a mensa, pranzi in auletta, cene, partite a ping-pong, di uscite e di tante risate insieme.
Ringrazio poi tutti i membri del "Pacchetto fisici on the world", perchè, nonostante la distanza che ci separa, siamo sempre più uniti: un grazie spe-

ciale va a Matteo, Aniello e Giuseppe, compagni di vacanze e di tante risate insieme e un grazie speciale va ad Agnese, per i consigli dati soprattutto in questi ultimi mesi. Grazie ragazzi, siete dei supertori!
Infine, ringrazio la mia famiglia e i miei genitori, perchè, nonostante tutte le mie lamentele, mi hanno sempre sostenuta.
Grazie.

Bibliography

[1] Planck Collaboration, P. A. R. Ade, N. Aghanim, C. Armitage-Caplan, M. Arnaud, M. Ashdown, F. Atrio-Barandela, J. Aumont, C. Baccigalupi, A. J. Banday, and et al. Planck 2013 results. XX. Cosmology from Sunyaev-Zeldovich cluster counts. *ArXiv e-prints*, March 2013.

[2] Raul Jimenez, P. Thejll, U. Jorgensen, J. MacDonald, and B. Pagel. Ages of globular clusters: a new approach. *Mon.Not.Roy.Astron.Soc.*, 282:926–942, 1996.

[3] L. Amendola and S. Tsujikawa. *Dark Energy: Theory and Observations*. 2010.

[4] E.L. Wright, S.S. Meyer, C.L. Bennett, N.W. Boggess, E.S. Cheng, et al. Interpretation of the Cosmic Microwave Background radiation anisotropy detected by the COBE differential microwave radiometer. *Astrophys.J.*, 396:L13–L18, 1992.

[5] Komatsu et. al. [WMAP collaboration]. *Astrophys. J. Suppl*, 192(18), 2011.

[6] Daniel J. Eisenstein et al. Detection of the baryon acoustic peak in the large-scale correlation function of SDSS luminous red galaxies. *Astrophys.J.*, 633:560–574, 2005.

[7] Lauren Anderson et al. The clustering of galaxies in the SDSS-III Baryon Oscillation Spectroscopic Survey: Baryon Acoustic Oscillations in the Data Release 10 and 11 galaxy samples. *Mon.Not.Roy.Astron.Soc.*, 441:24–62, 2014.

[8] Michael J. Mortonson, David H. Weinberg, and Martin White. Dark Energy: A Short Review. 2013.

[9] B.Ratra and J. Peebles. *Phys. Rev. D*, 37(128), 1988.

[10] Joshua A. Frieman, Christopher T. Hill, Albert Stebbins, and Ioav Waga. Cosmology with ultralight pseudo Nambu-Goldstone bosons. *Phys.Rev.Lett.*, 75:2077–2080, 1995.

[11] R.R. Caldwell, Rahul Dave, and P.J. Steinhardt. Quintessential cosmology: Novel models of cosmological structure formation. *Astrophys.Space Sci.*, 261:303–310, 1998.

[12] Bruce A. Bassett, Shinji Tsujikawa, and David Wands. Inflation dynamics and reheating. *Rev.Mod.Phys.*, 78:537–589, 2006.

[13] Edmund J. Copeland, Andrew R Liddle, and David Wands. Exponential potentials and cosmological scaling solutions. *Phys.Rev.*, D57:4686–4690, 1998.

[14] David Wands, Edmund J. Copeland, and Andrew R. Liddle. Exponential potentials, scaling solutions and inflation. 1993.

[15] Andrew R. Liddle and Robert J. Scherrer. A Classification of scalar field potentials with cosmological scaling solutions. *Phys.Rev.*, D59:023509, 1999.

[16] Paul J. Steinhardt, Li-Min Wang, and Ivaylo Zlatev. Cosmological tracking solutions. *Phys.Rev.*, D59:123504, 1999.

[17] Sean M. Carroll. Quintessence and the rest of the world. *Phys.Rev. Lett.*, 81, 1998.

[18] Jean-Philippe Uzan. Varying Constants, Gravitation and Cosmology. *Living Rev.Rel.*, 14:2, 2011.

[19] Jean-Philippe Uzan. Fundamental constants and tests of general relativity: Theoretical and cosmological considerations. 2009.

[20] Clifford M. Will. The confrontation between general relativity and experiment. *Living Rev. Rel.*, 4:4, 2001.

[21] Y. Su, Blayne R. Heckel, E.G. Adelberger, J.H. Gundlach, M. Harris, et al. New tests of the universality of free fall. *Phys.Rev.*, D50:3614–3636, 1994.

[22] R.D. Peccei, J. Sola, and C. Wetterich. Adjusting the Cosmological Constant Dynamically: Cosmons and a New Force Weaker Than Gravity. *Phys.Lett.*, B195:183, 1987.

[23] Thibault Damour and Freeman Dyson. The Oklo bound on the time variation of the fine structure constant revisited. *Nucl.Phys.*, B480:37–54, 1996.

[24] Justin Khoury. Theories of Dark Energy with Screening Mechanisms. 2010.

[25] Justin Khoury and Amanda Weltman. Chameleon cosmology. *Phys.Rev.*, D69:044026, 2004.

[26] Philippe Brax, C. van de Bruck, A.C. Davis, J. Khoury, and A. Weltman. Chameleon dark energy. *AIP Conf.Proc.*, 736:105–110, 2005.

[27] A.I. Vainshtein. To the problem of nonvanishing gravitation mass. *Phys.Lett.*, B39:393–394, 1972.

[28] Cedric Deffayet, G.R. Dvali, Gregory Gabadadze, and Arkady I. Vainshtein. Nonperturbative continuity in graviton mass versus perturbative discontinuity. *Phys.Rev.*, D65:044026, 2002.

[29] G.R. Dvali, Gregory Gabadadze, and Massimo Porrati. 4-D gravity on a brane in 5-D Minkowski space. *Phys.Lett.*, B485:208–214, 2000.

[30] Alberto Nicolis, Riccardo Rattazzi, and Enrico Trincherini. The Galileon as a local modification of gravity. *Phys.Rev.*, D79:064036, 2009.

[31] Massimo Pietroni. Dark energy condensation. *Phys.Rev.*, D72:043535, 2005.

[32] Keith A. Olive and Maxim Pospelov. Environmental dependence of masses and coupling constants. *Phys.Rev.*, D77:043524, 2008.

[33] Kurt Hinterbichler and Justin Khoury. Symmetron Fields: Screening Long-Range Forces Through Local Symmetry Restoration. *Phys.Rev.Lett.*, 104:231301, 2010.

[34] Laura Taddei, Riccardo Catena, and Massimo Pietroni. Spherical collapse and halo mass function in the symmetron model. *Phys.Rev.*, D89:023523, 2014.

[35] Kurt Hinterbichler, Justin Khoury, Aaron Levy, and Andrew Matas. Symmetron Cosmology. *Phys.Rev.*, D84:103521, 2011.

[36] B. Bertotti, L. Iess, and P. Tortora. A test of general relativity using radio links with the Cassini spacecraft. *Nature*, 425:374, 2003.

[37] Philippe Brax, Anne-Christine Davis, and Baojiu Li. Modified Gravity Tomography. *Phys.Lett.*, B715:38–43, 2012.

[38] Junpu Wang, Lam Hui, and Justin Khoury. No-Go Theorems for Generalized Chameleon Field Theories. *Phys.Rev.Lett.*, 109:241301, 2012.

[39] Philippe Brax, Anne-C. Davis, Baojiu Li, Hans A. Winther, and Gong-Bo Zhao. Systematic simulations of modified gravity: chameleon models. *JCAP*, 1304:029, 2013.

[40] Baojiu Li, Gong-Bo Zhao, and Kazuya Koyama. Exploring Vainshtein mechanism on adaptively refined meshes. *JCAP*, 1305:023, 2013.

[41] Anne-Christine Davis, Baojiu Li, David F. Mota, and Hans A. Winther. Structure Formation in the Symmetron Model. *Astrophys.J.*, 748:61, 2012.

[42] Philippe Brax, Anne-Christine Davis, Baojiu Li, Hans A. Winther, and Gong-Bo Zhao. Systematic Simulations of Modified Gravity: Symmetron and Dilaton Models. *JCAP*, 1210:002, 2012.

[43] James E. Gunn and III Gott, J. Richard. On the Infall of Matter into Clusters of Galaxies and Some Effects on Their Evolution. *Astrophys.J.*, 176:1–19, 1972.

[44] T. Padmanabhan. Structure formation in the universe. *Cambridge Univ. Press*, 1993.

[45] J.A. Peacock. Cosmological physics. *Cambridge Univ. Press*, 1999.

[46] Ofer Lahav, Per B. Lilje, Joel R. Primack, and Martin J. Rees. Dynamical effects of the cosmological constant. *Mon.Not.Roy.Astron.Soc.*, 251:128–136, 1991.

[47] F. Pace, J.-C. Waizmann, and M. Bartelmann. Spherical collapse model in dark energy cosmologies. *Mon.Not.Roy.Astron.Soc.*, 406:1865, 2010.

[48] Nico Wintergerst and Valeria Pettorino. Clarifying spherical collapse in coupled dark energy cosmologies. *Phys.Rev.*, D82:103516, 2010.

[49] Chung-Pei Ma and Edmund Bertschinger. Cosmological perturbation theory in the synchronous and conformal Newtonian gauges. *Astrophys.J.*, 455:7–25, 1995.

[50] Philippe Brax and Patrick Valageas. Impact on the power spectrum of Screening in Modified Gravity Scenarios. *Phys.Rev.*, D88(2):023527, 2013.

[51] Michele Maggiore and Antonio Riotto. The Halo Mass Function from Excursion Set Theory. I. Gaussian fluctuations with non-Markovian dependence on the smoothing scale. *Astrophys.J.*, 711:907–927, 2010.

[52] Ravi K. Sheth and Giuseppe Tormen. Large scale bias and the peak background split. *Mon.Not.Roy.Astron.Soc.*, 308:119, 1999.

[53] Fabian Schmidt, Marcos Vinicius Lima, Hiroaki Oyaizu, and Wayne Hu. Non-linear Evolution of f(R) Cosmologies III: Halo Statistics. *Phys.Rev.*, D79:083518, 2009.

[54] H. Weyl. *Annalen Phys.*, 59(101), 1919.

[55] A. S. Eddington. The mathematical theory of relativity. *Cambridge Univ. Press*, 1923.

[56] S. Capozziello, V.F. Cardone, S. Carloni, and A. Troisi. Curvature quintessence matched with observational data. *Int.J.Mod.Phys.*, D12:1969–1982, 2003.

[57] Sean M. Carroll, Vikram Duvvuri, Mark Trodden, and Michael S. Turner. Is cosmic speed - up due to new gravitational physics? *Phys.Rev.*, D70:043528, 2004.

[58] Luca Amendola. Scaling solutions in general nonminimal coupling theories. *Phys.Rev.*, D60:043501, 1999.

[59] Jean-Philippe Uzan. Cosmological scaling solutions of nonminimally coupled scalar fields. *Phys.Rev.*, D59:123510, 1999.

[60] Nicola Bartolo and Massimo Pietroni. Scalar tensor gravity and quintessence. *Phys.Rev.*, D61:023518, 2000.

[61] Richard P. Woodard. Avoiding dark energy with 1/r modifications of gravity. *Lect.Notes Phys.*, 720:403–433, 2007.

[62] G. W. Horndeski. *Int.J.Th.Phys.*, 10, 1974.

[63] C. Deffayet, Xian Gao, D.A. Steer, and G. Zahariade. From k-essence to generalised Galileons. *Phys.Rev.*, D84:064039, 2011.

[64] M. Gasperini and G. Veneziano. Pre - big bang in string cosmology. *Astropart.Phys.*, 1:317–339, 1993.

[65] L. Amendola, M. Kunz, and D. Sapone. Measuring the dark side (with weak lensing). *JCAP*, 4:13, April 2008.

[66] Antonio De Felice, Tsutomu Kobayashi, and Shinji Tsujikawa. Effective gravitational couplings for cosmological perturbations in the most general scalar-tensor theories with second-order field equations. *Phys.Lett.*, B706:123–133, 2011.

[67] Alessandra Silvestri, Levon Pogosian, and Roman V. Buniy. A practical approach to cosmological perturbations in modified gravity. 2013.

[68] Luca Amendola, Simone Fogli, Alejandro Guarnizo, Martin Kunz, and Adrian Vollmer. Model-independent constraints on the cosmological anisotropic stress. *Phys.Rev.*, D89:063538, 2014.

[69] Laura Taddei and Luca Amendola. A cosmological exclusion plot: Towards model-independent constraints on modified gravity from current and future growth rate data. 2014.

[70] Michael Doran and Georg Robbers. Early dark energy cosmologies. *JCAP*, 0606:026, 2006.

[71] V. Pettorino, L. Amendola, and C. Wetterich. How early is early dark energy? *arXiv:1301.5279*, January 2013.

[72] Y. Gong. Growth factor parametrization and modified gravity. *Phys. Rev. D*, 78, 2008.

[73] Tatsuya Narikawa and Kazuhiro Yamamoto. Characterizing the linear growth rate of cosmological density perturbations in an f(R) model. *Phys. Rev.*, D81:043528, 2010.

[74] Koichi Hirano, Zen Komiya, and Hisato Shirai. Constraining Galileon gravity from observational data with growth rate. *Prog.Theor.Phys.*, 127:1041–1056, 2012.

[75] K. Shi, Y.F. Huang, and T. Lu. Constraining dark energy using observational growth rate data. *Phys.Lett.*, B717:299–306, 2012.

[76] Edward Macaulay, Ingunn Kathrine Wehus, and Hans Kristian Eriksen. A Lower Growth Rate from Recent Redshift Space Distortions than Expected from Planck. 2013.

[77] Lado Samushia, Beth A. Reid, Martin White, Will J. Percival, Antonio J. Cuesta, et al. The Clustering of Galaxies in the SDSS-III Baryon Oscillation Spectroscopic Survey (BOSS): measuring growth rate and geometry with anisotropic clustering. 2013.

[78] Natalia A. Arkhipova, Olga Avsajanishvili, Tina Kahniashvili, and Lado Samushia. Growth Rate in the Dynamical Dark Energy Models. 2014.

[79] Heinrich Steigerwald, Julien Bel, and Christian Marinoni. Probing non-standard gravity with the growth index: a background independent analysis. *JCAP*, 1405:042, 2014.

[80] Martin Kunz and Domenico Sapone. Dark Energy versus Modified Gravity. *Phys.Rev.Lett.*, 98:121301, 2007.

[81] Surhud More, Hironao Miyatake, Rachel Mandelbaum, Masahiro Takada, David Spergel, et al. The Weak Lensing Signal and the Clustering of BOSS Galaxies: Cosmological Constraints. 2014.

[82] David Rapetti, Chris Blake, Steven W. Allen, Adam Mantz, David Parkinson, et al. A combined measurement of cosmic growth and expansion from clusters of galaxies, the CMB and galaxy clustering. *Mon.Not.Roy.Astron.Soc.*, 432:973, 2013.

[83] P.A.R. Ade et al. Planck 2013 results. XVI. Cosmological parameters. *arXiv:1303.5076*, 2013.

[84] Luca Amendola and Domenico Tocchini-Valentini. Stationary dark energy: The Present universe as a global attractor. *Phys.Rev.*, D64:043509, 2001.

[85] H. Nariai. Gravitational Instability in the Brans-Dicke Cosmology. *Progress of Theoretical Physics*, 42, 1969.

[86] Frank Könnig, Yashar Akrami, Luca Amendola, Mariele Motta, and Adam R. Solomon. Stable and unstable cosmological models in bimetric massive gravity. *Phys.Rev.*, D90:124014, 2014.

[87] R. Laureijs, J. Amiaux, S. Arduini, J. . Auguères, J. Brinchmann, R. Cole, M. Cropper, C. Dabin, L. Duvet, A. Ealet, and et al. Euclid Definition Study Report. *ArXiv e-prints*, October 2011.

[88] Ippocratis D. Saltas, Ignacy Sawicki, Luca Amendola, and Martin Kunz. Scalar anisotropic stress as signature of correction to gravitational waves. 2014.

[89] N. Kaiser. Clustering in real space and in redshift space. *Mon.Not.Roy.Astron.Soc.*, 227:1–27, 1987.

[90] Scott Dodelson. *Modern Cosmology.* Academic Press, 2003.

[91] Luca Amendola et al. Cosmology and fundamental physics with the Euclid satellite. *Living Rev.Rel.*, 16:6, 2013.

[92] Florian Beutler, Chris Blake, Matthew Colless, D. Heath Jones, Lister Staveley-Smith, et al. The 6dF Galaxy Survey: z 0 measurement of the growth rate and sigma-8. *Mon.Not.Roy.Astron.Soc.*, 423:3430–3444, 2012.

[93] Lado Samushia, Will J. Percival, and Alvise Raccanelli. Interpreting large-scale redshift-space distortion measurements. *Mon.Not.Roy.Astron.Soc.*, 420:2102–2119, 2012.

[94] Rita Tojeiro, W.J. Percival, J. Brinkmann, J.R. Brownstein, D. Eisenstein, et al. The clustering of galaxies in the SDSS-III Baryon Oscillation Spectroscopic Survey: measuring structure growth using passive galaxies. *Mon.Not.Roy.Astron.Soc.*, 424:2339–2344, 2012.

[95] Chris Blake, Sarah Brough, Matthew Colless, Carlos Contreras, Warrick Couch, et al. The WiggleZ Dark Energy Survey: Joint measurements of the expansion and growth history at z ¡ 1. *Mon.Not.Roy.Astron.Soc.*, 425:405–414, 2012.

[96] S. de la Torre, L. Guzzo, J.A. Peacock, E. Branchini, A. Iovino, et al. The VIMOS Public Extragalactic Redshift Survey (VIPERS). Galaxy clustering and redshift-space distortions at z=0.8 in the first data release. 2013.

[97] Will J. Percival et al. The 2dF Galaxy Redshift Survey: Spherical harmonics analysis of fluctuations in the final catalogue. *Mon.Not.Roy.Astron.Soc.*, 353:1201, 2004.

[98] Chia-Hsun Chuang and Yun Wang. Modeling the Anisotropic Two-Point Galaxy Correlation Function on Small Scales and Improved Measurements of $H(z)$, $D_A(z)$, and $\beta(z)$ from the Sloan Digital Sky Survey DR7 Luminous Red Galaxies. *Mon.Not.Roy.Astron.Soc.*, 435:255–262, 2013.

[99] Chia-Hsun Chuang, Francisco Prada, Florian Beutler, Daniel J. Eisenstein, Stephanie Escoffier, et al. The clustering of galaxies in the SDSS-III Baryon Oscillation Spectroscopic Survey: single-probe measurements from CMASS and LOWZ anisotropic galaxy clustering. 2013.

[100] Florian Beutler et al. The clustering of galaxies in the SDSS-III Baryon Oscillation Spectroscopic Survey: Testing gravity with redshift-space distortions using the power spectrum multipoles. 2013.

[101] Beth A. Reid, Hee-Jong Seo, Alexie Leauthaud, Jeremy L. Tinker, and Martin White. A 2.5space clustering of SDSS-III CMASS galaxies. 2014.

[102] Cinzia Di Porto and Luca Amendola. Observational constraints on the linear fluctuation growth rate. *Phys. Rev.*, D77:083508, 2008.

[103] Athina Pouri, Spyros Basilakos, and Manolis Plionis. Precision growth index using the clustering of cosmic structures and growth data. *JCAP*, 1408:042, 2014.

[104] D. J. Kapner, T. S. Cook, E. G. Adelberger, J. H. Gundlach, B. R. Heckel, C. D. Hoyle, and H. E. Swanson. Tests of the Gravitational Inverse-Square Law below the Dark-Energy Length Scale. *Physical Review Letters*, 98(2):021101, January 2007.

[105] Antonio De Felice and Shinji Tsujikawa. f(R) theories. *Living Rev.Rel.*, 13:3, 2010.

[106] L. G. Jaime, L. Patino, and M. Salgado. f(R) Cosmology revisited. *ArXiv e-prints*, June 2012.